

1 **Aerosol-Driven Precipitation Modification: Spatiotemporal Heterogeneity in**  
2 **Precipitation Microphysics and Vertical Profiles over China's Megacity Clusters**

删除[phy]: Vertical Structures

3 Heyuan Peng<sup>1</sup>, Xiong Hu<sup>2\*</sup>, Weihua Ai<sup>1\*</sup>, Zhen Li<sup>1</sup>, Shensen Hu<sup>1</sup>, Junqi Qiao<sup>1</sup>,  
4 Xianbin Zhao<sup>1</sup>

← 设置格式[phy]: 正文文本

5 <sup>1</sup>*College of Meteorology and Oceanography, National University of Defense*  
6 *Technology, Changsha, China*

7 <sup>2</sup>*College of Basic Education, National University of Defense Technology, Changsha,*  
8 *China*

删除[phy]: Basic Education College

9 *\*Corresponding authors: X. Hu (huxiong18@nudt.edu.cn) and W. Ai*  
10 *(aiweihua@nudt.edu.cn)*

11  
12 **ABSTRACT**

13 As crucial atmospheric components, aerosols influence precipitation through  
14 complex microphysical mechanisms and exhibit spatiotemporal heterogeneity. This  
15 study investigates aerosol effects on precipitation vertical profiles and microphysical  
16 characteristics across four Chinese urban clusters (the Beijing–Tianjin–Hebei (BTH),  
17 Yangtze River Delta (YRD), Yangtze River Middle Reaches (YRM), and Pearl River  
18 Delta (PRD)), including sensitivities to meteorological factors. Initially, the principal  
19 findings elucidate three fundamental attributes of precipitation differences: regional  
20 disparities surpass seasonal variations in magnitude; heightened aerosol loadings  
21 mitigate regional precipitation discrepancies, particularly during the spring and  
22 summer seasons; convective precipitation exhibits greater regional and seasonal  
23 variability than stratiform precipitation. Furthermore, the findings indicate that  
24 aerosols exert an influence on precipitation through microphysical processes,  
25 encompassing the growth via condensation on cloud condensation nuclei, coalescence

删除[phy]: vertical structures

26 growth, semi-direct effect, and moisture competition. These phenomena exhibit  
27 distinct variations that are influenced by spatial and temporal factors, along with the  
28 particular type of aerosols present. Specifically, convective precipitation in the BTH  
29 region is dominated by the semi-direct effect and invigoration effect of dust aerosols,  
30 whereas the YRD and PRD are more influenced by hygroscopic sea salt aerosols and  
31 the YRM by fine aerosol particles. Furthermore, RH promotes condensation and  
32 coalescence processes by replenishing water vapor, particularly under low aerosol  
33 loading. However, CAPE plays a dual role: it enhances precipitation by intensifying  
34 cloud development and suppresses it through particle break-up driven by dynamics.  
35 The present study elucidates the mechanisms of spatio-temporal modulation  
36 underlying aerosol-precipitation interactions, offering a scientific foundation for the  
37 refinement of climate models within urban agglomerations.

38 **Key words:** GPM DPR, MERRA-2, Aerosols, Precipitation Structure, Urban  
39 Agglomerations

40

41

## 42 1. Introduction

43 Aerosols modulate clouds and precipitation primarily through Aerosol-Radiation  
44 Interactions (ARI) and Aerosol-Cloud Interactions (ACI) (IPCC,2013; IPCC, 2021),  
45 which subsequently affect the intensity, frequency, and spatiotemporal distribution of  
46 precipitation (Rosenfeld et al., 2008). These interactions involve complex multiscale,  
47 multi-factor coupling effects with profound implications for regional hydrological  
48 cycles, extreme weather events, and climate systems (Li et al., 2016, 2019;  
49 Ramanathan et al., 2001; Zhao et al., 2018, 2020). Therefore, elucidating  
50 aerosol-driven precipitation mechanisms remains one of the key objectives in  
51 atmospheric science, (IPCC, 2013; IPCC, 2021). As a central component of this  
52 modulation framework, the ACI describes the process by which aerosols function as

设置格式[phy]: (中文)中文(简体)

删除[phy]: These mechanisms

删除[phy]: processes

删除[phy]: Therefore, one of the most important problems facing atmospheric research is the clarification of aerosol-driven precipitation mechanisms

设置格式[phy]: (中文)中文(简体)

删除[phy]: In this framework

删除[phy]: mechanism

53 ice nuclei (IN) and cloud condensation nuclei (CCN), modifying cloud microphysical  
54 processes to indirectly modify the type and distribution of precipitation intensity  
55 (IPCC, 2013; Gettelman, 2015). Specifically, these modified cloud microphysical  
56 processes include cloud droplet spectrum distribution, phase transition efficiency, and  
57 precipitation formation pathways (Xie et al., 2013). The phenomenon known as the  
58 Twomey Effect (the First Indirect Effect) describes how higher aerosol loadings  
59 increase cloud droplet concentration, while decreasing their effective radius ( $r_e$ ) and  
60 increasing cloud albedo (Twomey, 1974). In addition, the Cloud Lifetime Effect  
61 (Second Indirect Effect), aerosol-induced reduction in  $r_e$  suppresses precipitation  
62 initiation, whereas prolonging cloud lifetime (Albrecht, 1989). The subsequent  
63 Semi-Direct Effect shortens cloud lifetime through another mechanism: absorptive  
64 aerosols within clouds heat the atmosphere by absorbing shortwave radiation, thus  
65 promoting droplet evaporation (Ackerman et al., 2000; Huang et al., 2014). Despite  
66 the established understanding of primary mechanisms, significant uncertainties  
67 remain in quantifying aerosol impacts on precipitation. This complexity stems from  
68 the highly nonlinear and diverse nature of aerosol-precipitation responses (Chang et  
69 al., 2015), which are modulated by aerosol loading, type, vertical distribution, and  
70 local meteorological conditions (Fan et al., 2007; Storer et al., 2010), leading to  
71 pronounced regional variations (Li et al., 2025a; Xiao et al., 2025). Furthermore,  
72 external synoptic conditions, entrainment, and other in-cloud meteorological factors,  
73 particularly that surrounding clouds and challenging to be measured, can affect the  
74 aerosol effect on clouds and precipitation (Chen et al., 2025; Lee et al., 2008;  
75 Stevens and Feingold, 2009; Sun et al., 2023; Zhao et al., 2024).

76 Recent research has extensively examined aerosol-induced modifications of  
77 precipitation structures in major urban clusters across China (Guo et al., 2018; Sun  
78 and Zhao, 2021; Zhao et al., 2025). China's major urban agglomerations,  
79 Beijing–Tianjin–Hebei (BTH), Yangtze River Delta (YRD), Pearl River Delta (PRD),  
80 and Yangtze River Middle Reaches (YRM), characterized by dense populations,  
81 robust economies, and severe aerosol pollution, are critical regions for studying how  
82 aerosol effects manifest at regional scales. Previous research has been conducted on

删除[phy]: These

删除[phy]: Known as the Twomey Effect

设置格式[phy]: (中文) 中文(简体)

删除[phy]: the number of

删除[phy]: s

删除[phy]: ,

设置格式[phy]: (中文) 中文(简体)

删除[phy]: The Semi-Direct Effect is another way in which absorptive aerosols can shorten cloud lifetime by heating the atmosphere through the absorption of shortwave radiation, which accelerates droplet evaporation

删除[phy]: There are still many unknowns surrounding the measurement of aerosol impacts on precipitation, even though the primary mechanisms of aerosol-precipitation interactions are documented

删除[phy]: This is due to the diversity and highly nonlinear characteristics of aerosol-precipitation responses

删除[phy]: jointly regulated

删除[phy]: Furthermore, external synoptic conditions modulate the ACI process

设置格式[phy]: 缩进: 首行缩进: 2 字符

删除[phy]: Significant research in recent years has focused on aerosol-induced modifications of precipitation structures in key regions of China

设置格式[phy]: (中文) 中文(简体)

83 aerosol-driven precipitation patterns in more general areas, such as the North China  
84 Plain (Sun et al., 2023), South China (Chen et al., 2025), and East China (Wen et al.,  
85 2023) under different seasonal and precipitation type conditions (Day et al., 2018;  
86 Guo et al., 2019). These studies have consistently confirmed that the modulation  
87 effects of aerosols on clouds and precipitation exhibit pronounced regional  
88 heterogeneity (Guo et al., 2017, 2019; Li et al., 2019; Sun and Zhao, 2021). However,  
89 the underlying physical mechanisms, particularly the cloud microphysical processes  
90 responsible for these disparate regional responses, are not yet fully understood.  
91 Moreover, numerical models show substantial instability in precipitation capture  
92 (Zhang et al., 2024), and simulation capabilities exhibit inherent asymmetries  
93 (Snively and Gallus, 2014). The comparability of findings across regions and seasons  
94 is often limited by methodological and data source differences, which sustain  
95 scientific debates. Adopting a unified analytical framework is therefore essential to  
96 reconcile these discrepancies and enable systematic comparison.

设置格式[phy]: (中文) 中文(简体)

设置格式[phy]: (中文) 中文(简体)

删除[phy]: analysis of specific seasons or precipitation types is frequently limited without considering meteorological drivers.

设置格式[phy]: (中文) 中文(简体)

设置格式[phy]: (中文) 中文(简体)

删除[phy]: In summary, methodological divergences and data source variations across studies have yielded divergent conclusions with persistent controversies, precluding robust cross-regional comparisons of aerosol impacts on precipitation structures. Therefore, it is essential to develop consistent techniques for the collection and interpretation of aerosol-precipitation data.

设置格式[phy]: 缩进: 首行缩进: 0 毫米

97  
98 The Global Precipitation Measurement (GPM) mission extends and advances the  
99 Tropical Rainfall Measuring Mission (TRMM). Compared with TRMM's  
100 single-frequency Precipitation Radar (PR), the Dual-frequency Precipitation Radar  
101 (DPR) onboard the GPM core observatory demonstrates higher sensitivity and  
102 provides more accurate three-dimensional precipitation structure. This increase  
103 markedly enhances precipitation detection capabilities at mid-to high latitudes (Hou et  
104 al., 2014). Furthermore, comparisons between GPM DPR precipitation data and  
105 observations from ground-based radars and meteorological stations (Chandrasekar  
106 and Le, 2015; Lasser et al., 2019; Sun et al., 2020) validated the substantial agreement  
107 across all three platforms. Moreover, a robust concordance in surface precipitation  
108 patterns and brilliant band height was noted between DPR data and the  
109 high-resolution NICAM 3.5 km model (Kotsuki et al., 2023), hence reinforcing data  
110 dependability.

111 Additionally, Modern-Era Retrospective Analysis for Research and Applications  
112 Version 2 (MERRA-2) significantly improves the accuracy of aerosol vertical

113 distributions and optical properties through assimilation of multi-source satellite and  
114 ground-based observations (Buchard et al., 2017; Chang et al., 2015). Building on the  
115 reliable precipitation data from GPM DPR, researchers analyzed aerosol impacts on  
116 precipitation vertical profile, microphysical characteristics, and extreme  
117 hydrometeorological events using integrated MERRA-2 aerosol and DPR  
118 precipitation datasets (Ji and Tian, 2024; Jiang et al., 2023; Sun et al., 2022).  
119 Furthermore, compared with the ECMWF Re-Analysis-Interim (ERA-Interim), the  
120 European Centre for Medium-Range Weather Forecasts Reanalysis Version 5  
121 (ERA-5) offers significantly improved spatiotemporal resolution, yielding superior  
122 environmental parameters (Zhao et al., 2021). This enhancement facilitates its  
123 widespread utilization in research investigating the impact of aerosol on precipitation  
124 structure (Dong et al., 2018; Guo et al., 2018; Pravia-Sarabia et al., 2023).

删除[phy]: structure

125 (Peng et al., 2025) conducted a focused investigation into the effects of fine and  
126 coarse aerosols on summer precipitation processes within the YRD region. The results  
127 indicated that coarse aerosols suppress convective precipitation by competing for  
128 moisture, whereas fine aerosols enhance precipitation by forming small droplet  
129 clusters with condensational and coalescence growth. However, precipitation  
130 characteristics vary significantly across different regions and seasons, which can be  
131 attributed to differences in aerosol types, concentrations, and meteorological  
132 conditions. Therefore, this study integrates precipitation, aerosol, and environmental  
133 data from four major urban agglomerations (the BTH, YRD, YRM, and PRD)  
134 between 2014 and 2023. A multi-source DPR-MERRA-2-ERA5 dataset was  
135 constructed to systematically analyze the impact of aerosol on precipitation properties  
136 and microphysical processes. In addition, this study systematically examines how  
137 aerosol-precipitation interactions are modulated by thermodynamic and dynamic  
138 conditions. This unified methodology facilitates a comprehensive, cross-regional, and  
139 cross-seasonal comparison of aerosol impacts on precipitation and cloud microphysics  
140 across China's major urban agglomerations.

删除[phy]: the interactions between aerosol and precipitation structures are further investigated under varying thermodynamic and dynamic conditions

141 The remainder of this paper is organized as follows: Section 2 introduces the data  
142 and methods. Section 3 examines aerosol influences on precipitation structure and

删除[phy]: .

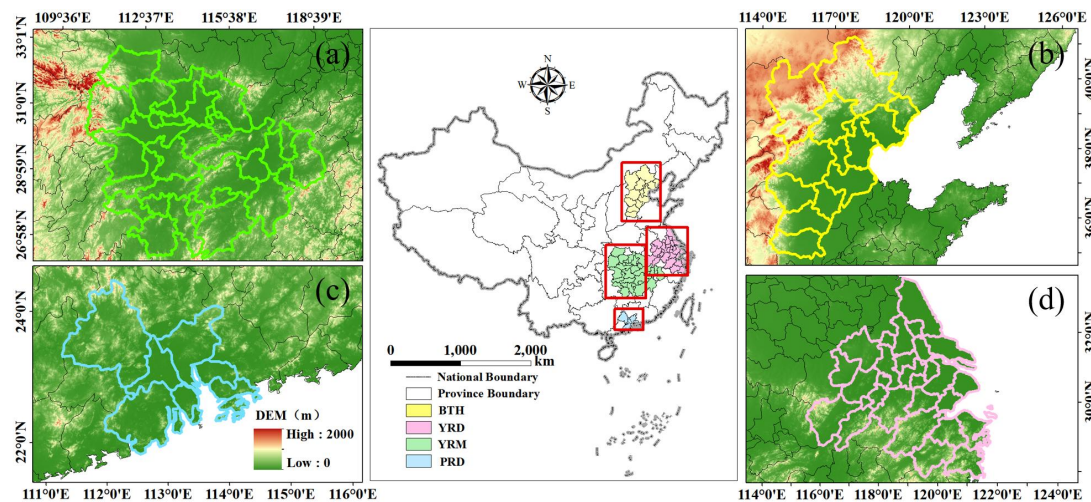
143 properties. Section 4 conducts an analysis of aerosol effects on the microphysical  
144 processes of precipitation. Section 5 investigates meteorological effects on  
145 aerosol-precipitation interactions. Section 6 summarizes the conclusions of this study  
146 and Section 7 discusses the limitations and shortcomings of this research.

## 147 **2. Data and Methods**

### 148 **2.1 Study area**

149 The YRM urban cluster (Fig. 1a) is situated between 26°N–32.5°N and  
150 110.5°E–118.3°E, inside a humid subtropical monsoon region characterized by  
151 concentrated summer precipitation. The BTH region (36°N–41.6°N, 113.5°E–119.9°E;  
152 Fig. 1b) exhibits a temperate semi-humid continental monsoon climate, with summer  
153 comprising over 67% of the annual precipitation and spring characterized by  
154 numerous dust events (Zhai et al., 2022). The PRD cluster (21.7°N–23.8°N,  
155 112°E–115.4°E; Fig. 1c) exhibits a South Asian tropical marine monsoon climate,  
156 characterized by 85% of annual precipitation occurring from April to September,  
157 frequently exacerbated by typhoons (Guo et al., 2018). Dominated by the Taihu Plain  
158 (27.9°N–33.3°N, 117.5°E–122.7°E; Fig. 1d), the YRD exhibits a humid subtropical  
159 monsoon climate characterized by concentrated spring–summer precipitation,  
160 including prolonged June–July Meiyu–front rainfall (Liu et al., 2017). Fig. 1 shows  
161 the spatial distribution of all four urban agglomerations. It is noteworthy that the  
162 selected urban agglomerations are primarily situated in plains and basins, thus  
163 minimizing the potential confounding effects of complex terrain on the  
164 aerosol-cloud-precipitation interactions analyzed in this study.

删除[phy]: the



165  
 166 **Fig. 1. Geographical distribution of four urban agglomerations over (a) the Yangtze**  
 167 **River Middle Reaches, (b) Beijing–Tianjin–Hebei, (c) Pearl River Delta, and (d)**  
 168 **Yangtze River Delta (d), which is superimposed with elevation,** (source: GS(2024)  
 169 0650). Publisher ’ s remark: please note that the above figure contains disputed  
 170 territories.

删除[phy]: Geographical location and elevation map of the Yangtze River Middle Reaches (a), Beijing–Tianjin–Hebei (b), Pearl River Delta (c), and Yangtze River Delta (d) urban agglomeration

## 171 2.2 GPM DPR Precipitation Data

172 Mounted on the core satellite, the DPR transmits at the Kuband (13.6 GHz) and  
 173 Kaband (35.5 GHz) frequencies, achieving a nadir horizontal resolution of 5 km to  
 174 detect three–dimensional precipitation structures from the surface to an altitude of 22  
 175 km (Hou et al., 2014). This study utilized the GPM Level 2 DPR (2ADPR) standard  
 176 product, Version 07, which employs two unique antenna scanning modes: the  
 177 High–Sensitivity Scan (HS) and the Full Scan (FS). A significant alteration in Version  
 178 07, compared to Version 06, entails a shift in the KaPR scanning pattern from the  
 179 inner swath to the outer swath configuration. This change aligns the KaPR scanning  
 180 mode with that of KuPR.

删除[phy]: Given the relatively low frequency of winter precipitation events and frequent occurrence of solid precipitation in northern regions,

181 This study focuses on liquid precipitation processes detectable by the GPM DPR  
 182 during spring (March–May), summer (June–August), and autumn  
 183 (September–November) from 2014 to 2023. The parameters analyzed in this study  
 184 include: The near–surface Rain Rate (nsRR), Rain Rate (RR), Storm Top Height  
 185 (STH), Liquid Water Path (LWP), Ice Water Path (IWP), DSD, and radar reflectivity

设置格式[phy]: (中文) 中文(简体)

设置格式[phy]: (中文) 中文(简体)

设置格式[phy]: (中文) 中文(简体)

设置格式[phy]: (中文) 中文(简体)

删除[phy]: this study focuses on precipitation data during spring (March–May), summer (June–August), and autumn (September–November) from 2014 to 2023

186 factor ( $Z_e$ ). The DSD includes two parameters: mass-weighted diameter ( $D_m$ ) and  
187 normalized DSD intercepts ( $N_w$ ).

### 188 **2.3 MERRA-2 Aerosol Data**

189 This study utilized the MERRA-2 atmospheric reanalysis dataset, updated in  
190 2017 and released by NASA's Global Modeling and Assimilation Office (GMAO).  
191 By assimilating multi-source observations with numerical modeling techniques, this  
192 dataset characterizes the column mass concentrations of five aerosol types: dust (DU),  
193 sea salt (SS), sulfate ( $SO_4$ ), black carbon (BC), and organic carbon (OC), and their  
194 corresponding AOD. The data feature a global spatial coverage at a horizontal grid  
195 resolution of  $0.625^\circ \times 0.5^\circ$  (longitude  $\times$  latitude), with temporal products available at  
196 hourly intervals. It is noteworthy that the matched aerosol data are those within 1 hour  
197 prior to the onset of precipitation events.

198 The spatial and seasonal distributions of aerosol composition over China's  
199 megacity clusters, are detailed in Figs. S3-S8. Overall, the BTH region is  
200 characterized by a high burden of DUA (Figs. S3-S8b), particularly during spring. In  
201 contrast, the PRD region shows a pronounced signal of SSA, especially in spring and  
202 summer (Figs. S3-S8d). Figs. S3-S8 (f-g) show that loadings of both absorbing and  
203 scattering aerosols are markedly elevated in the BTH region, in contrast to the  
204 discernibly lower concentrations observed in the PRD. These characteristic  
205 distributions provide a fundamental basis for interpreting the region-specific  
206 aerosol-precipitation mechanisms discussed in subsequent sections.

### 207 **2.4 ERA-5 Data**

208 Environmental data for this study were acquired from the ERA5 reanalysis  
209 dataset. Through the coupled assimilation of multi-source satellite observations,  
210 ground-based measurements, and numerical forecasting systems, this product  
211 provides multidimensional climate parameters that span the surface-to-stratopause  
212 column spatial resolution of  $0.25^\circ \times 0.25^\circ$  and temporal resolution of 1 hour (Hersbach  
213 et al., 2020). This investigation utilizes two key parameters: Relative Humidity (RH)  
214 at 850\_hPa and Convective Available Potential Energy (CAPE).

设置格式[phy]: 缩进: 首行缩进: 2 字符

设置格式[phy [2]]: (中文) 中文(简体)

删除[phy [2]]: It is noteworthy that the aerosol data matched are those prior to precipitation events

设置格式[phy]: (中文) 中文(简体)

## 215 **2.5 Classification Methods**

216 Prior to data analysis, the DPR, MERRA-2, and ERA5 datasets were subjected to  
217 spatiotemporal matching using the best-proximity method. Subsequently,  
218 precipitation pixels were screened using the connectivity method (Hu et al., 2022,  
219 2024; Peng et al., 2025; Wang et al., 2024), applying a minimum threshold of four  
220 contiguous pixels (nsRR) to define valid precipitation systems (Liu and Zipser, 2015).  
221 This study categorized precipitation into stratiform and convective types based on the  
222 2ADPR classification criteria, excluding shallow convection events (defined by the  
223 0°C isotherm attitude below STH more than 1 km) from convective precipitation (Liu  
224 and Zipser, 2015). It is noteworthy that shallow convection precipitation constitutes a  
225 non-negligible proportion of the convective events in our dataset (Table S1). This  
226 prevalence underscores the necessity of our methodological decision to exclude these  
227 events. Aerosol classification followed the total AOD thresholds: Low AOD, [0, 0.3);  
228 Medium AOD, [0.3, 0.6); and High AOD, [0.6, ~). In terms of aerosol classification,  
229 BCA, OCA, and SO<sub>4</sub>A were categorized as fine aerosol particles, whereas SSA and  
230 DUA were classified as coarse aerosol particles.

设置格式[phy]: (中文) 中文(简体)

设置格式[phy]: (中文) 中文(简体)

设置格式[phy]: 非上标/ 下标

231 Fig. S1 illustrates the cumulative distribution functions (CDFs) of the RH and  
232 CAPE throughout the four urban agglomerations for meteorological conditioning.  
233 Given the higher similarity in RH distributions among the YRD, YRM, and PRD  
234 versus distinct BTH characteristics, the YRD-YRM-PRD RH data were unified (red  
235 dashed line; Fig. S1a-c). Conversely, the BTH-YRD-YRM exhibited comparable  
236 CAPE distributions, and the PRD showed significantly higher values. Thus, the  
237 BTH-YRD-YRM CAPE data were combined (red dashed line; Fig. S1d-f). To  
238 balance methodological consistency with regional specificity, the classification  
239 strategy implemented distinct groupings: RH was classified separately for the BTH  
240 region, whereas the YRD, YRM, and PRD shared a unified RH classification.  
241 Similarly, CAPE maintained independent classification for the PRD, whereas BTH,  
242 YRD, and YRM employed combined CAPE classification, as visualized by the red  
243 dashed lines in Fig. S1. Moreover, to prevent feature ambiguity from adjacent  
244 samples, three percentile tiers were defined using the CDFs thresholds: low

245 (0%–30%), medium (35%–65%), and high (70%–100%), with 30–35% and 65–70%  
246 as buffer zones to avoid adjacent–sample ambiguity.

## 247 **2.6 Normalized difference calculation**

248 To quantify regional and seasonal differences in precipitation parameters, the  
249 BTH region and spring season were set as the benchmark for normalizing variations.

250 The X denote target precipitation parameter, which includes nsRR, STH, LWP, IWP,  
251 and precipitation efficiency index (PEI). The fractional changes (DIFF<sub>region</sub>, in %) for  
252 each parameter in the YRD, YRM, and PRD regions relative to BTH were calculated  
253 as follows:

$$254 \text{DIFF}_{\text{region}} = \frac{X_{\text{region}} - X_{\text{BTH}}}{X_{\text{BTH}}} * 100\% \quad (1)$$

255 Beyond regional differences, the fractional seasonal changes (DIFF<sub>season</sub>, in %)  
256 for precipitation parameters were calculated as:

$$257 \text{DIFF}_{\text{season}} = \frac{X_{\text{season}} - X_{\text{spring}}}{X_{\text{spring}}} * 100\% \quad (2)$$

258 where DIFF<sub>region</sub> represents the normalized differences for the YRD, YRM, and  
259 PRD relative to BTH, respectively; DIFF<sub>season</sub> denotes the normalized seasonal  
260 differences when comparing summer and autumn to spring. X<sub>BTH</sub> and X<sub>spring</sub> represent  
261 the reference value of the target precipitation parameter in the BTH and spring,  
262 respectively. X<sub>region</sub> denotes the precipitation parameter values for the YRD, YRM,  
263 and PRD regions, respectively, and X<sub>season</sub> represents the precipitation parameter  
264 values in the seasons being compared to spring.

## 265 **3 Influence of aerosols on precipitation structure and properties**

### 266 **3.13.1 Correlation changes of precipitation parameters with aerosols**

267 To investigate aerosol impacts on convective and stratiform precipitation  
268 characteristics across the four urban agglomerations, five precipitation parameters  
269 were selected: nsRR, STH, LWP, IWP, and the precipitation efficiency index (PEI).

270 The PEI is quantifies the efficiency of cloud water to precipitation conversion, with  
271 higher values denoting a greater proportion of cloud water being transformed into

删除[phy]: In order t

设置格式[phy]: (中文) 中文(简体)

设置格式[phy]: 突出显示

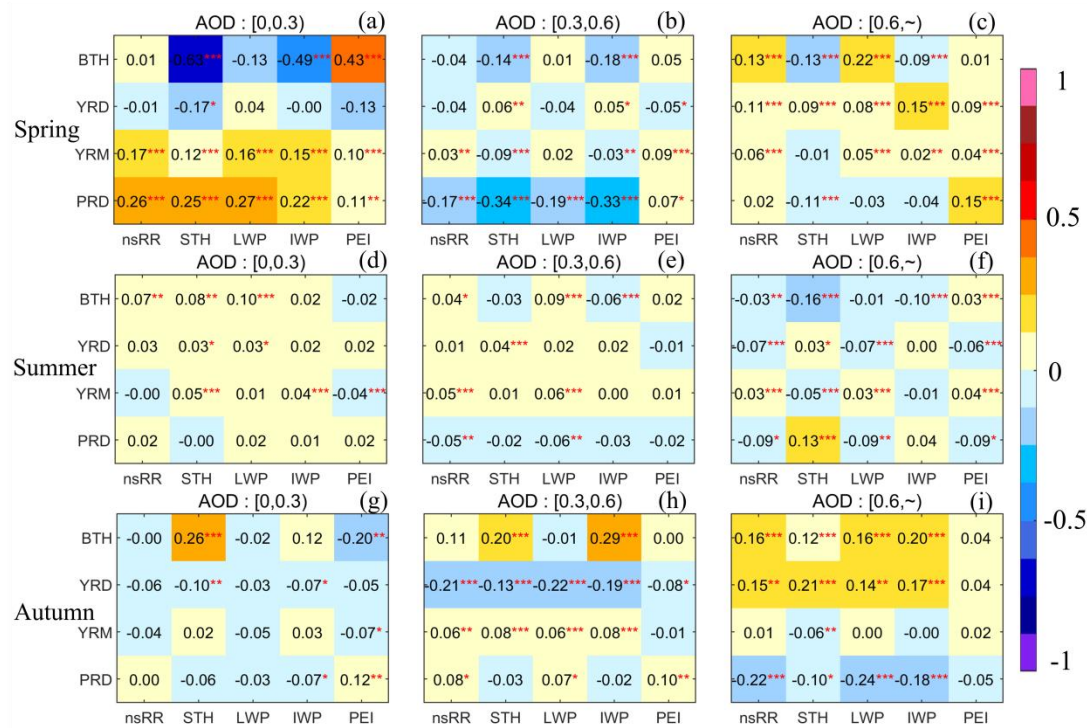
设置格式[phy]: 缩进: 首行缩进: 1 字符

272 | rainfall. Following Hu et al. (2022) and scaled by 1000 for enhanced readability, PEI  
273 is defined as:

$$274 \quad \text{PEI} = \frac{\text{nsRR}}{\text{CWP}} = \frac{\text{nsRR}}{(\text{LWP} + \text{IWP})} * 1000 \quad (3)$$

275 In the resulting heat map of convective precipitation (Fig. 2), individual cells  
276 exhibit Spearman correlation coefficients that quantify the relationship between AOD  
277 and key meteorological parameters. For spring convective precipitation (Fig. 2a–c),  
278 the BTH exhibits significant negative correlations with the STH and IWP under low  
279 aerosol loading, whereas showing a significant positive correlation with PEI. The  
280 YRD displays patterns similar to those of the BTH: negative correlations at low  
281 aerosol loading shift to positive correlations with precipitation parameters as aerosol  
282 loading increases. In contrast, both the YRM and PRD show consistently positive  
283 correlations under low aerosol loading (Fig. 2a). However, the PRD demonstrates  
284 pronounced negative correlations at moderate loading, whereas the YRM maintains  
285 positive correlations at high aerosol loading. Summer (Fig. 2d–g): Under low (high)  
286 AOD conditions, consistent positive (negative) correlations prevail across all study  
287 regions (Fig. 2d). At moderate aerosol loading levels, the PRD shifts to a negative  
288 correlation, whereas the other three regions retain a positive correlation (Fig. 2e).  
289 Autumn (Fig. 2g–i): the YRD exhibits pronounced negative correlations under  
290 low–to–moderate AOD thresholds. Conversely, the BTH and YRD (PRD)  
291 demonstrate positive (negative) correlations under high AOD levels. Overall, the  
292 precipitation under varying aerosol loading exhibits pronounced seasonal and regional  
293 disparities, demonstrating nonlinear characteristics in their relationships.

删除[phy]: a crucial metric for measuring the efficiency of precipitation formation in clouds, indicating the effectiveness of converting cloud water into precipitation. Higher PEI values indicate enhanced precipitation efficiency, which is characterized by a greater conversion of cloud water into rainfall



294

295 **Fig. 2.** Spearman correlation coefficients between AOD and precipitation parameters  
 296 for convective precipitation across regions and seasons under the three AOD regimes.  
 297 Color gradients (from yellow to blue) encode the correlation strength and direction,  
 298 and asterisks denote statistical significance (\*:  $p < 0.05$ , \*\*:  $p < 0.01$ , \*\*\*:  $p < 0.001$ ).

299 Spearman correlation coefficients are computed to characterize the precipitation  
 300 parameters in stratiform precipitation (Fig. S9), similar to that of convective  
 301 precipitation (Fig. 2). Overall, the PRD exhibits the strongest similarity between the  
 302 stratiform and convective precipitation parameters in the correlation with AOD. In  
 303 contrast, the BTH, YRD, and YRM resemble convective precipitation characteristics  
 304 under moderate to high aerosol loading, but show reduced similarity under low  
 305 aerosol loading, particularly in the BTH.

306 Given the dominant roles of DUA in BTH and SSA in PRD (Figs. S2-S8), the  
 307 further investigated how these key aerosol types distinctly modulate precipitation.  
 308 Correlation analyses reveal that DUA is significantly positively correlated with both  
 309 IWP and STH in the convective precipitation (Fig. S10), indicating an invigoration of  
 310 ice-phase processes. This suggests that DUA, acting as efficient IN, promote the  
 311 glaciation and vertical development of convective clouds, consistent with the  
 312 invigoration effect (Rosenfeld et al., 2008). In contrast, the impact of DUA on

设置格式[phy]: Text, 行距: 1.5 倍行距

删除[phy]: 3

设置格式[phy]: (中文) 中文(简体)

设置格式[phy]: (中文) 中文(简体)

设置格式[phy]: (中文) 中文(简体)

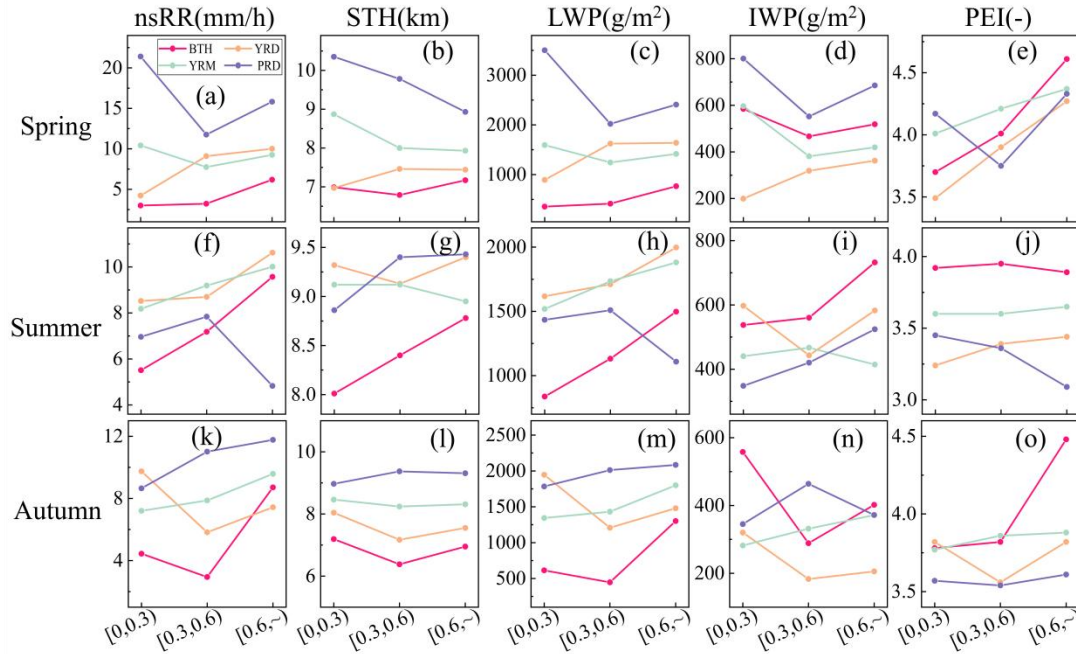
313 stratiform precipitation is substantially weaker and more variable. This promotional  
314 mechanism, facilitated by ice-nucleating ability of DUA, stands in contrast to  
315 precipitation-suppressing semi-direct effect, highlighting the complex and  
316 multi-faceted nature of DUA impacts on different precipitation types.

### 317 *3.2 Changes in the characteristics of precipitation parameters associated with* 318 *aerosols*

删除[phy]: structural

319 Fig. 3 illustrates the seasonal mean values of the convective precipitation  
320 parameters for nsRR, STH, LWP, IWP, and PEI across AOD intervals. During spring  
321 (Fig. 3a–e), the BTH and YRD regions exhibit similar responses, with nsRR, STH,  
322 LWP, and PEI demonstrating persistent enhancement as the aerosol burden increases.  
323 In contrast, the YRM and PRD manifest nonlinear features: nsRR, LWP, and IWP  
324 experience initial suppression before rebounding at elevated AOD levels. Summer  
325 observations (Fig. 3f–j) reveal predominantly linear positive relationships between  
326 aerosol loading and precipitation parameters in the BTH, YRD, and YRM regions.  
327 However, the PRD diverges sharply, displaying inverted V-shaped responses in the  
328 nsRR, STH, LWP, and PEI. Autumn analysis (Fig. 3k–o) reveals consistent increases  
329 in the YRM and PRD with aerosol enhancement, whereas the BTH and YRD exhibit  
330 a pattern of initial decline followed by a subsequent increase.

331 The regional comparisons indicate that the differences of the precipitation  
332 parameters are mitigated under moderate to high aerosol loading conditions (Table 1).  
333 For instance, at low aerosol loading, the fractional changes in spring nsRR reach  
334  $\text{DIFF}_{\text{PRD}}=613\%$  and  $\text{DIFF}_{\text{YRM}}=247.33\%$ , whereas high aerosol loading reduces these  
335 to  $\text{DIFF}_{\text{PRD}}=155\%$  and  $\text{DIFF}_{\text{YRM}}=49.6\%$  (Table 1). These results highlight that  
336 increasing aerosol loading can moderately alleviate regional disparities in  
337 precipitation characteristics. Furthermore, the BTH exhibits notably higher IWP and  
338 PEI values, indicating enhanced ice-phase processes and superior precipitation  
339 conversion efficiency, as evidenced by the negative  $\text{DIFF}_{\text{YRD}}$ ,  $\text{DIFF}_{\text{YRM}}$ , and  $\text{DIFF}_{\text{PRD}}$   
340 values.



341

342 **Fig. 3.** Average point line plots of nsRR, STH, LWP, IWP, and PEI under three AOD  
 343 conditions for convective precipitation across the four regions and three seasons. Each  
 344 subplot employs color-coding ( BTH-red, YRD-yellow, YRM-green, and  
 345 PRD-purple) with the x-axis denoting AOD bins ([0,0.3), [0.3,0.6), [0.6, ~)) and the  
 346 y-axis representing parameter magnitudes. "-" indicates dimensionless (after scaling  
 347 by 1000).

348 **Table 1.** Normalized regional differences in convective precipitation during the  
 349 spring season. Units: nsRR (mm/h), STH (km), LWP ( $\text{g}/\text{m}^2$ ), IWP ( $\text{g}/\text{m}^2$ ).

	AOD	BTH	YRD $\text{DIFF}_{\text{YRD}}$	YRM $\text{DIFF}_{\text{YRM}}$	PRD $\text{DIFF}_{\text{PRD}}$
nsRR	[0,0.3)	3	4.23+41.00%	10.42+247.33%	21.4+613.33%
	[0.3,0.6)	3.23	9.1+181.73%	7.75+139.94%	11.76+264.09%
	[0.6,~)	6.19	10.01+61.71%	9.26+49.60%	15.82+155.57%
STH	[0,0.3)	6.99	6.97-0.29%	8.87+26.90%	10.35+48.07%
	[0.3,0.6)	6.79	7.46+9.87%	8+17.82%	9.78+44.04%
	[0.6,~)	7.17	7.44+3.77%	7.93+10.60%	8.93+24.55%
LWP	[0,0.3)	355.11	892.42+151.31%	1593.58+348.76%	3501.97+886.16%
	[0.3,0.6)	414.57	1622.99+291.49%	1242.87+199.80%	2019.85+387.22%
	[0.6,~)	765	1639.19+114.27%	1415.35+85.01%	2407.82+214.75%

设置格式[phy]: 字体: (默认) Times New Roman, (中文) 宋体, 小四

	[0,0.3)	584.6	199.12-65.94%	596.38+2.02%	800.57+36.94%
IWP	[0.3,0.6)	466.54	319.12-31.60%	381.24-18.28%	552.17+18.35%
	[0.6,~)	518.72	362.2-30.17%	419.48-19.13%	685.27+32.11%
	[0,0.3)	3.7	3.49-5.68%	4.01+8.38%	4.17+12.70%
PEI	[0.3,0.6)	4.01	3.9-2.74%	4.21+4.99%	3.75-6.48%
	[0.6,~)	4.61	4.27-7.38%	4.37-5.21%	4.33-6.07%

350 To further characterize the stratiform precipitation parameters (nsRR, STH, LWP,  
351 IWP, and PEI), the seasonal mean values across aerosol loading levels are presented  
352 in Fig. S4 through point–line plots that were formatted consistently with those in Fig.  
353 3.

354 For spring (Fig. S4a–e), the BTH, YRD, and YRM exhibit continuously  
355 increasing trends in nsRR, LWP, and IWP with increasing aerosol loading.  
356 Conversely, the PRD shows overall decreasing trends across most precipitation  
357 parameters. In summer (Fig. S4f–j), the BTH, YRD, and YRM demonstrate linear  
358 increases in nsRR and LWP means as aerosol loading rises. However, the PRD  
359 exhibits nonlinear trends: initial increases followed by decreases in nsRR, STH, LWP,  
360 and IWP means, a pattern consistent with its convective precipitation behavior. In  
361 autumn (Fig. S4k–o): monotonically rising trends in nsRR, LWP, and IWP are shown  
362 by the YRD and YRM, whereas the BTH and PRD display decreasing and then  
363 increasing trends in nsRR, IWP, and PEI, indicating an increase in aerosol loading.  
364 Additionally, the fractional changes in stratiform precipitation indicate that an  
365 increase in aerosol loading moderately reduces regional disparities during regional  
366 normalized difference comparisons, particularly in the spring and summer  
367 (Tables [S4-6](#)). For instance, in the PRD region during spring (Table [S4](#)), the  
368  $DIFF_{PRD}$  values for IWP are 208.16%, 141.06%, and 34.13%, corresponding to AOD  
369 ranges of [0, 0.3), [0.3, 0.6), and [0.6, ~), respectively. The seasonal normalized  
370 differences indicate significant ice-phase processes but weak liquid-phase processes  
371 across various regions during spring. To summarize, aerosols influence the average  
372 values of precipitation parameters, displaying characteristics that differ across

删除[phy]: 3

删除[phy]: 5

删除[phy]: 3

删除[phy]:

373 spatiotemporal scales and precipitation types. Furthermore, precipitation parameters  
374 exhibit greater regional than seasonal variation. In particular, within the 270  $DIFF_{region}$   
375 samples, 41 (constituting 15.2%) exhibited values exceeding 100%, whereas among  
376 the 240  $DIFF_{season}$  samples, only 10 (representing 4.2%) demonstrated such a  
377 phenomenon (Tables S.2-8). Additionally, convective precipitation shows larger  
378 magnitude changes across seasons and regions than stratiform precipitation.

删除[phy]: 1

删除[phy]: 7

### 379 3.3 Changes in the vertical *profiles* of precipitation associated with aerosols

删除[phy]: *structure*

380 To further investigate the vertical structure of precipitation, Fig. 4 presents the  
381 vertical distributions of the mean  $Z_e$ ,  $D_m$ ,  $N_w$ , and RR for convective precipitation  
382 under varying AOD loadings and seasons. Overall, the mean  $Z_e$ ,  $N_w$ , and RR values  
383 generally increase with decreasing height, whereas  $D_m$  exhibits an initial decrease  
384 followed by an increase. In addition, the PRD displays a markedly higher RR than the  
385 BTH, YRD, and YRM in spring, but lower RR in summer. This seasonal contrast may  
386 be attributed to the abundant moisture supply during the pre-rainy season in South  
387 China (Chen and Luo, 2018), versus significant precipitation suppression in summer  
388 caused by hygroscopic aerosol-induced moisture competition (Guo et al., 2017).  
389 Furthermore, Chen et al. (2025) observed that a moderate CAPE in the PRD summer  
390 may lead to diminished precipitation.

设置格式[phy]: 缩进: 首行缩进: 2 字符

391 Despite a complex influence that varies with season and precipitation type, DUA  
392 in the BTH region exhibit a consistent negative correlation with  $N_w$  (Fig. S12b-e).  
393 This negative correlation could be attributed to the semi-direct effect of DUA,  
394 whereby the absorption of solar radiation heats the atmosphere, thus promoting cloud  
395 droplet evaporation and suppressing droplet concentrations. The negative relationship  
396 with RR and  $D_m$  is particularly evident in stratiform precipitation under  
397 low-to-medium aerosol loadings (Fig. S12d). For convective precipitation, the  
398 influence of DUA is seasonally modulated, showing a negative correlation in summer  
399 but a positive correlation in spring and autumn. Meanwhile, in the PRD region (Fig.  
400 S12g-l), SSA during spring and summer are consistently positively correlated with

删除[phy]: (Chen and Luo, 2018)

设置格式[phy]: (中文) 中文(简体)

设置格式[phy]: 字体: 倾斜, (中文) 中文(简体)

设置格式[phy]: 字体: 倾斜, 下标, (中文) 中文(简体)

设置格式[phy]: (中文) 中文(简体)

设置格式[phy]: (中文) 中文(简体)

设置格式[phy]: (中文) 中文(简体)

设置格式[phy]: 字体: 倾斜

设置格式[phy]: 字体: 倾斜, 下标

设置格式[phy]: (中文) 中文(简体)

设置格式[phy]: (中文) 中文(简体)

设置格式[phy]: (中文) 中文(简体)

401 precipitation parameters. These statistically significant relationships further  
402 corroborate the proposed type-specific mechanisms.

403 As shown in Fig. 4a-b, in spring, the RR and  $Z_e$  for the lower layers (<5 km)  
404 increase linearly with aerosol loading in the BTH and YRD but display  
405 non-monotonic trends (initial suppression followed by enhancement) in the YRM and  
406 PRD, consistent with Fig. 3a-e. In the BTH region, which is characterized by a high  
407 concentration of DUA(Figs. S2-8). Sun and Zhao, (2021), attributed similar  
408 phenomena to the radiative effect of aerosols enhancing atmospheric instability and  
409 triggering earlier precipitation. However, absorptive DUA can also suppress  
410 precipitation through the semi-direct effect, whereby radiative heating promotes cloud  
411 droplet evaporation. Furthermore, DUA can serve as efficient IN, promoting the  
412 glaciation and vertical development of convective clouds. These findings highlight the  
413 dual role of DUA, with the net precipitation effect being determined by the balance  
414 between invigoration and suppression. The YRD exhibits a more abundant water  
415 vapor supply (Fig. S1a): Increased aerosol loadings supply additional CCN and IN,  
416 providing more condensation nuclei for cloud droplet formation and thereby  
417 enhancing precipitation. With increasing aerosol loadings, the aerosol population in  
418 the YRM region shifts from low-concentration large cloud particles to  
419 high-concentration small cloud particles dominance (Fig. 4c-d). The resulting  
420 reduction in  $r_e$  suppresses initial precipitation, thereby prolonging cloud lifetime,  
421 which in turn fosters further cloud development and ultimately enhances precipitation.  
422 The PRD precipitation patterns resemble those of the YRM, although hygroscopic  
423 SSA exert a stronger influence (Fig. S2a). At low AOD (with an SSA proportion of  
424 26.32%), moisture from South China's pre-rainy season and hygroscopic giant CCN  
425 derived from sea salt promote spring precipitation growth (Guo et al., 2022). As AOD  
426 increases, the SSA contribution declines rapidly, weakening its  
427 precipitation-promoting effect. However, with further AOD growth, the proportion of  
428 fine (notably hygroscopic OCA) aerosols rises (Fig. S2a), supplying more effective  
429 CCN to enhance the precipitation. Additionally, under low aerosol loadings, the lower

删除[phy]: 5

删除[phy]: 4

设置格式[phy]: (中文) 中文(简体)

删除[p hy]:

删除[phy]: This discrepancy may arise from the predominant influence of DUA on the spring AOD composition of the BTH region (Fig. S), whereby their semi-direct effect promotes

删除[p hy]: .

删除[phy]: Although the rising proportion of fine-mode aerosols mitigates dust-induced precipitation suppression as AOD increases, persistently low moisture availability in th

删除[p hy]:

删除[phy]:

设置格式[phy]: (中文) 中文(简体)

删除[phy]: With increasing AOD, the YRM transitions from low-concentration coarse particles to high-concentration fine particles (Fig. 4c-d). Inadequate moisture supply triggers t

删除[phy]: AOD conditions

430 atmosphere in the YRD (YRM) is dominated by high concentrations of smaller (larger)  
431 **raindrop particles (Fig. 4c-d).**

432 During summer (Fig. 4e-h), average vertical profiles (**below 5 km**) of RR and  $Z_e$   
433 in the BTH, YRD, and YRM generally exhibit increasing linear trends with rising  
434 aerosol loading. Conversely, the PRD shows an initial increase followed by a decrease,  
435 which is consistent with the findings in Fig. 3f-j. Within the BTH, YRD, and YRM,  
436 low proportions of hygroscopic giant CCN (SSA) mean increasing aerosols boost  $N_w$   
437 and  $D_m$ , supplying more CCN and IN for cloud droplet formation. Coupled with  
438 ample summer moisture supply and dynamic forcing, cloud droplets are transported to  
439 higher altitudes (Fig. 3g), enhancing precipitation. During summer in the PRD, ample  
440 moisture is derived from the Indian Ocean. With low aerosol loading, the proportion  
441 of sea salt particles is elevated (23.83%). An increase in giant sea salt CCN loading  
442 triggers an anti-Twomey effect, characterized by a rise in  $D_m$  and a decline in  $N_w$ ,  
443 leading to intensified precipitation. Nevertheless, as aerosol loading escalates further,  
444 fine-mode particles predominate (93.9%; Fig. S2b), resulting in moisture competition  
445 becoming the principal mechanism inhibiting precipitation.

446 Consistent with Fig. 3k-o, during autumn the convective precipitation in the BTH  
447 and YRD initially decreases and then increases with rising aerosol loading (Fig. 4i-l).  
448 The magnitude of this increase is greater in the BTH than in the YRD. Conversely,  
449 RR exhibits monotonically increasing trends in the YRM and PRD. The underlying  
450 mechanisms are as follows. The BTH and YRD: Initial aerosol increase elevates  $N_w$   
451 while reducing  $D_m$  (Fig. 4k-l), suppressing precipitation via the Twomey effect.  
452 However, prolonged cloud lifetime promotes further cloud development (**Fig. 3l-m;**  
453 Albrecht, 1989; Rosenfeld et al., 2008; Zhao et al., 2024). Consequently, when  
454 aerosol loading continues rising, abundant CCN and IN become available for  
455 cloud-precipitation processes, ultimately enhancing precipitation. The YRM and PRD:  
456 The monotonic trends stem from greater autumn moisture availability versus the BTH  
457 and YRD (Fig. S1c), which supports cloud droplet condensational growth (Fig. 4k-l)  
458 and enhances collision-coalescence (Fig. 5a), collectively facilitating precipitation.

设置格式[phy]: (中文) 中文(简体)

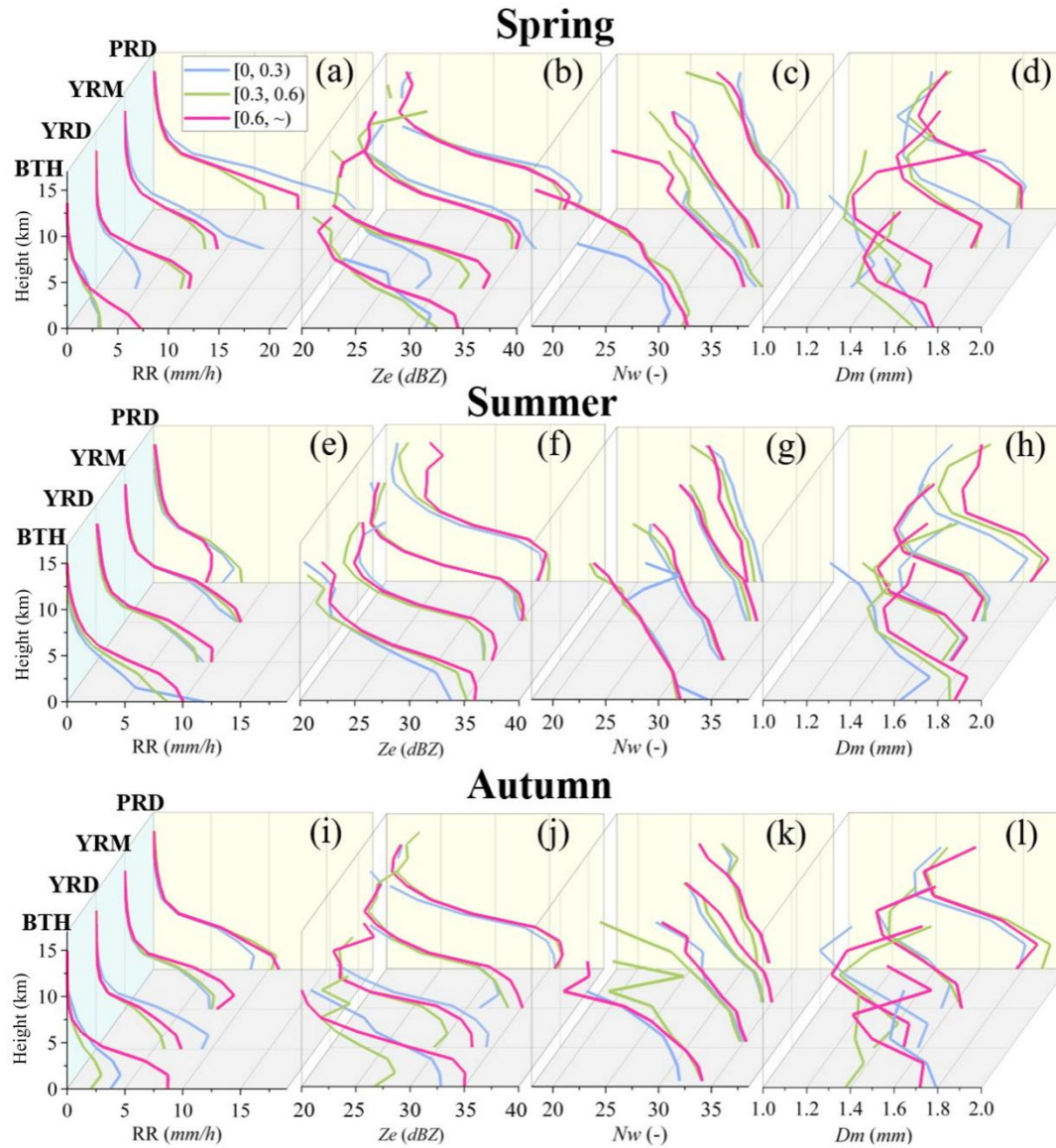
设置格式[phy]: 突出显示

删除[phy]: As aerosol loading increases, the Twomey effect emerges in the YRM, whereas the BTH and YRD exhibit the anti-Twomey effect.

删除[phy]: the

设置格式[phy]: (中文) 中文(简体)

删除[phy]: Consistent with the conclusions in Fig. 3k-o, autumn trends (Fig. 4i-l) show that precipitation in the BTH and YRD initially decreased and then increased with increasing aerosol loading, although the magnitude of the increase is increasing with rising aerosol loading, though the increase magnitude is larger in the BTH than in the YRD



459

460 **Fig. 4.** Vertical profiles of the average convective precipitation parameters  $Z_e$ ,  $D_m$ ,  $N_w$   
 461 and RR for different regions in different seasons under three AOD conditions  
 462 ( [0,0.3]—blue lines; [0.3,0.6]—green lines; [0.6, ~)—magenta lines ). Within each  
 463 subplot, line profiles are categorized into four regions: BTH, YRD, YRM, and PRD.

464 To enhance the characterization of the vertical profile and microphysical  
 465 processes of stratiform precipitation, Fig. S5 displays the mean vertical profiles of  $Z_e$ ,  
 466  $D_m$ ,  $N_w$ , and RR, similar to those in Fig. 4. A notable  $Z_e$  peak at an altitude of 5 km  
 467 corresponds to the 0 °C bright band signature, which is a distinctive indicator of the  
 468 hydrometeor phase transition and stratiform precipitation. Fig. S5a illustrates that the  
 469 PRD exhibits declining trends in RR and  $Z_e$ , diverging from the characteristics of

删除[phy]: structure

470 convective precipitation depicted in Fig. 4a–b. In the PRD, increasing aerosol loading  
471 induces a Twomey effect:  $N_w$  increases, accompanied by a decrease in  $D_m$  (Fig.  
472 S5c–d). This dominance of particle competition mechanisms at higher AOD loadings  
473 aligns with increasing OCA contributions (Fig. S2c–d), as light-absorbing OCAs  
474 suppress precipitation via semi-direct effects of shortwave radiation absorption.

475 During summer (Fig. S5 e–h), the BTH region displayed distinct patterns  
476 compared to the other three regions: RR decreases with increasing aerosol loading,  
477 whereas  $Z_e$  and  $D_m$  increase simultaneously. This suggests that higher aerosol loads  
478 increase cloud albedo (Garrett and Zhao, 2006; Twomey, 1974), thereby intensifying  
479 the smaller cloud particles evaporation and break-up (Fig. 5b), resulting in a decline  
480 in PEI (Fig. S4j). Concurrently, the increased abundance of hygroscopic  $\text{SO}_4\text{A}$  further  
481 depletes the atmospheric moisture. These combined effects lead to a notable reduction  
482 in precipitation within the BTH region. The summer stratiform precipitation responses  
483 of the PRD to aerosol loading resemble those of convective precipitation, whereas the  
484 YRD and YRM show negligible alterations in the vertical profiles, suggesting a low  
485 sensitivity of stratiform precipitation to aerosol loading.

#### 486 **4 Influence of aerosols on precipitation microphysical processes**

487 To validate the aforementioned microphysical processes, this study assesses  
488 near-surface precipitation mechanisms below the melting layer. The melting layer  
489 refers to the region where the ice phase of the hydrometeors transitions to the liquid  
490 phase during precipitation (Hu et al., 2024), and the analysis employs the  
491 categorization approach established by Kumjian and Prat (2014). This approach  
492 employs radar reflectivity ( $\Delta Z_e = Z_e^{1\text{km}} - Z_e^{3\text{km}}$ ) and raindrop size ( $\Delta D_m = D_m^{1\text{km}} - D_m^{3\text{km}}$ )  
493 differences between 1 km and 3 km above ground level. These metrics classify  
494 processes into four categories: size sorting evaporation, coalescence, break-up, and  
495 break-up coalescence balance. The extensive application of this methodology in  
496 precipitating cloud systems, demonstrates that coalescence and breakup processes  
497 are key mechanisms in cloud microphysics, (Chen et al., 2025; Hu et al., 2022; Wen  
498 et al., 2023; Zhou et al., 2022). Consequently, this analysis focuses exclusively on

删除[phy]: (Twomey et al., 1974; Garrett and Zhao, 2006)

删除[phy]: This suggests that higher aerosol loads enhance particle albedo, thereby intensifying the evaporation of smaller particles and the processes of break-up (Fig. 5b), such that while  $N_w$  remains stable, the PEI declines (Fig. S4j).

设置格式[phy]: 字体: 倾斜

设置格式[phy]: 字体: 倾斜, 下标

设置格式[phy [2]]: 字体: (默认) Times New Roman, (中文) 宋体, 小四

删除[phy [2]]: cloud precipitation

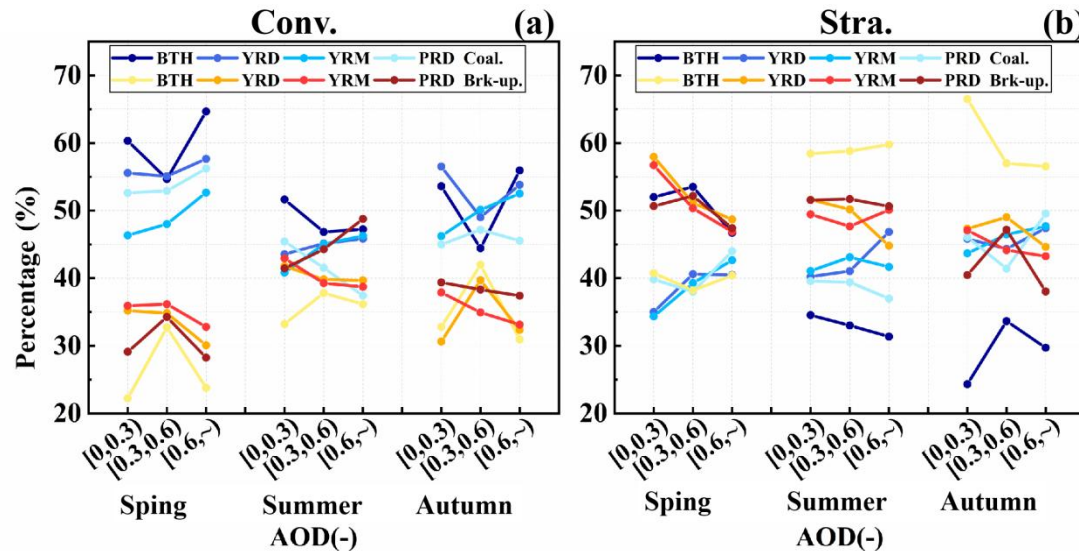
删除[phy]: The extensive application of this methodology demonstrates that coalescence and break-up processes dominate cloud microphysics

499 | coalescence and break-up mechanisms. Fig. 5 displays the coalescence and  
 500 break-up processes for convective and stratiform precipitation across regions and  
 501 seasons.

删除[phy]: these two

502 In convective precipitation (Fig. 5a), coalescence consistently dominates over  
 503 break-up across all regions, particularly during spring and autumn. With rising AOD  
 504 concentrations, the YRD, YRM, and PRD exhibit enhanced coalescence in spring,  
 505 whereas the PRD shows a decreasing-then-increasing trend in coalescence. In summer,  
 506 the proportions of coalescence and break-up remain comparable, whereas autumn  
 507 exhibits nonlinear responses in the BTH and YRD.

508 In stratiform precipitation (Fig. 5b), break-up generally exceeds coalescence,  
 509 with distinct seasonal patterns: in spring, the BTH exhibits increasing-then-decreasing  
 510 coalescence, whereas the PRD shows the opposite trend (aligning with divergent RR  
 511 patterns in Fig. S5a). During summer and autumn, BTH consistently shows notably  
 512 lower break-up than coalescence, which is one of the reasons why precipitation  
 513 continues to decline with increasing AOD loading in summer. The specific  
 514 microphysical influence process is explained in detail in Section 3.



515  
 516 **Fig. 5.** Average point line plots of coalescence and break-up processes in precipitation  
 517 across different regions and seasons (Spr.-Spring, Sum.-Summer, and Aut.-Autumn)  
 518 under three AOD conditions. Here, (a) represents convective precipitation, and (b)  
 519 represents stratiform precipitation. And "-" indicates dimensionless.

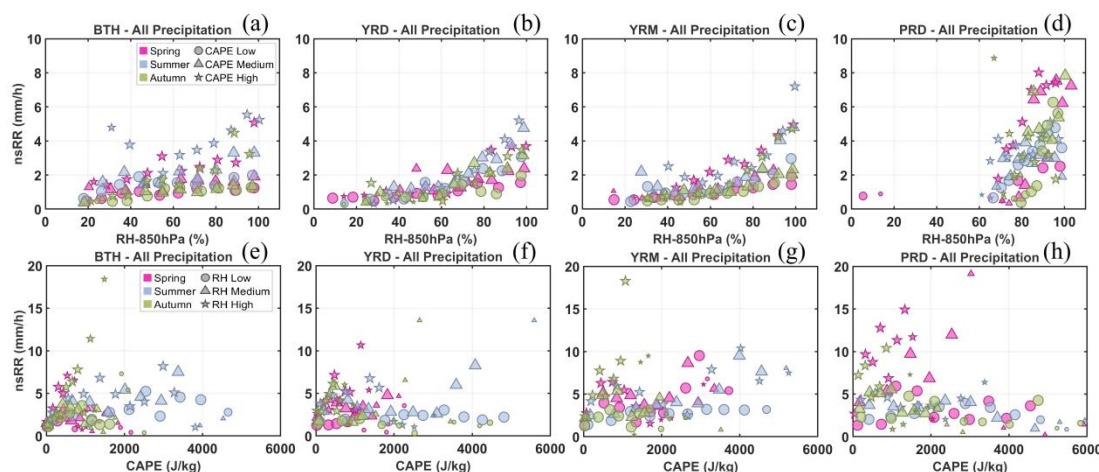
设置格式[phy]: 字体: 小四

## 520 5 Meteorological effects

### 521 5.1 Sensitivity of precipitation macroscopic parameters

522 Since precipitation processes are equally influenced by thermodynamic and  
523 dynamic environments, this study employs RH at 850\_hPa as a thermal influence  
524 factor and CAPE as a dynamic influence factor to examine aerosol sensitivity to these  
525 meteorological elements. Following the classification criteria established in Section  
526 2.5, RH and CAPE values were categorized into low, medium, and high levels.

527 Fist of all, as shown in Fig. 6 a–d, an increase in RH generally enhances the  
528 near-surface rain rate (nsRR), and the combination of high RH × high CAPE  
529 (indicated by ☆) tends to produce heavier precipitation. However, as the CAPE  
530 values (Fig. 6 e–h) continue to rise beyond 4000 J/kg, the nsRR shows a decreasing  
531 trend. Moreover, extremely high CAPE values are most often observed alongside  
532 moderate to low RH (indicated by ○ and △) conditions.



533 **Fig. 6.** nsRR as a function of RH-850 hPa (CAPE), stratified by season (color) and  
534 CAPE (RH) level (symbol), for all precipitation types (convective and stratiform) in  
535 the four regions. The symbol size is proportional to the sample size ([0,20), [20,45),  
536 [45,90), [90,~)).

538 Following the format of Fig. 3, Fig. 7 displayed point-line plots of convective  
539 precipitation parameters across regions under different RH and aerosol loading

删除[phy]: *Sensitivity analysis of aerosols to meteorological factors in precipitation parameters*

设置格式[phy]: 行距: 2 倍行距

设置格式[phy]: 字体: 小四, 非加粗

设置格式[phy]: 字体: 小四, 非加粗

设置格式[phy]: 字体: 小四, 非加粗

设置格式[phy]: 缩进: 首行缩进: 0 字符

设置格式[phy]: 字体: (中文) 宋体

设置格式[phy]: 缩进: 首行缩进: 0 字符, 孤行控制

设置格式[phy]: 字体: (中文) 宋体

设置格式[phy]: 字体: (中文) 宋体, 加粗, 字距调整: 1 磅

设置格式[phy]: 字体: (默认) Times New Roman, (中文) 宋体, 小四

设置格式[phy]: 字体: (默认) Times New Roman, (中文) 宋体, 小四

设置格式[phy]: 字体: (默认) Times New Roman, (中文) 宋体, 小四

设置格式[phy]: 字体: (默认) Times New Roman, (中文) 宋体, 小四

设置格式[phy]: 字体: (默认) Times New Roman, (中文) 宋体, 小四

设置格式[phy]: 字体: (默认) Times New Roman, (中文) 宋体, 小四

设置格式[phy]: 字体: (默认) Times New Roman, (中文) 宋体, 小四

设置格式[phy]: 字体: (默认) Times New Roman, (中文) 宋体, 小四

设置格式[phy]: 字体: (默认) Times New Roman, (中文) 宋体, 小四

设置格式[phy]: 字体: (中文) 宋体, 小四, 字体颜色: 自动设置

删除[phy]: 6

540 conditions. Notably, higher RH values consistently enhance mean precipitation  
541 parameters (nsRR, LWP, PEI) across all regions, whereas STH and IWP show  
542 inconsistent seasonal and regional variations. This suggests that elevated RH supplies  
543 additional moisture, thereby mitigating moisture competition effects.

544 In spring (Fig. 7a–e), rising RH values do not interfere with the established  
545 trends of the BTH across varying aerosol loadings: nsRR and LWP continue to rise  
546 with aerosol loading, yet STH and IWP exhibit persistent decrease-then-increase  
547 trajectories. Precipitation parameters in the YRD and YRM remain consistent with the  
548 characteristics observed in Fig. 3a–e. By contrast, the PRD displays distinct  
549 characteristics under moderate RH conditions. This indicates that aerosols exhibit  
550 greater sensitivity to RH in the spring convective precipitation of the PRD, whereas  
551 aerosol effects dominate over RH influences in the BTH, YRD, and YRM.

552 Under high RH during summer (Fig. 7f–j), the BTH response differs from that  
553 shown in Fig. 3f–j (characterized by a general increase in macroscopic precipitation  
554 parameters with aerosol loading); however, other regions remain consistent with prior  
555 trends in Fig. 3f–j. In autumn, observations (Fig. 7k–o) highlight inconsistent  
556 aerosol–precipitation relationships across the RH levels in the PRD. By contrast, the  
557 BTH, YRD, and YRM maintain nearly identical parameter responses.

558 The results indicate that RH sensitivity significantly influences  
559 aerosol-precipitation effects on convective precipitation in the PRD, whereas aerosol  
560 loading is the main factor affecting precipitation parameters in the other three regions.

删除[phy]: 6

设置格式[phy]: 字体: (默认) Times New Roman, (中文)  
宋体, 小四

设置格式[phy]: 字体: (默认) Times New Roman, (中文)  
宋体, 小四

设置格式[phy]: 字体: (默认) Times New Roman, (中文)  
宋体, 小四

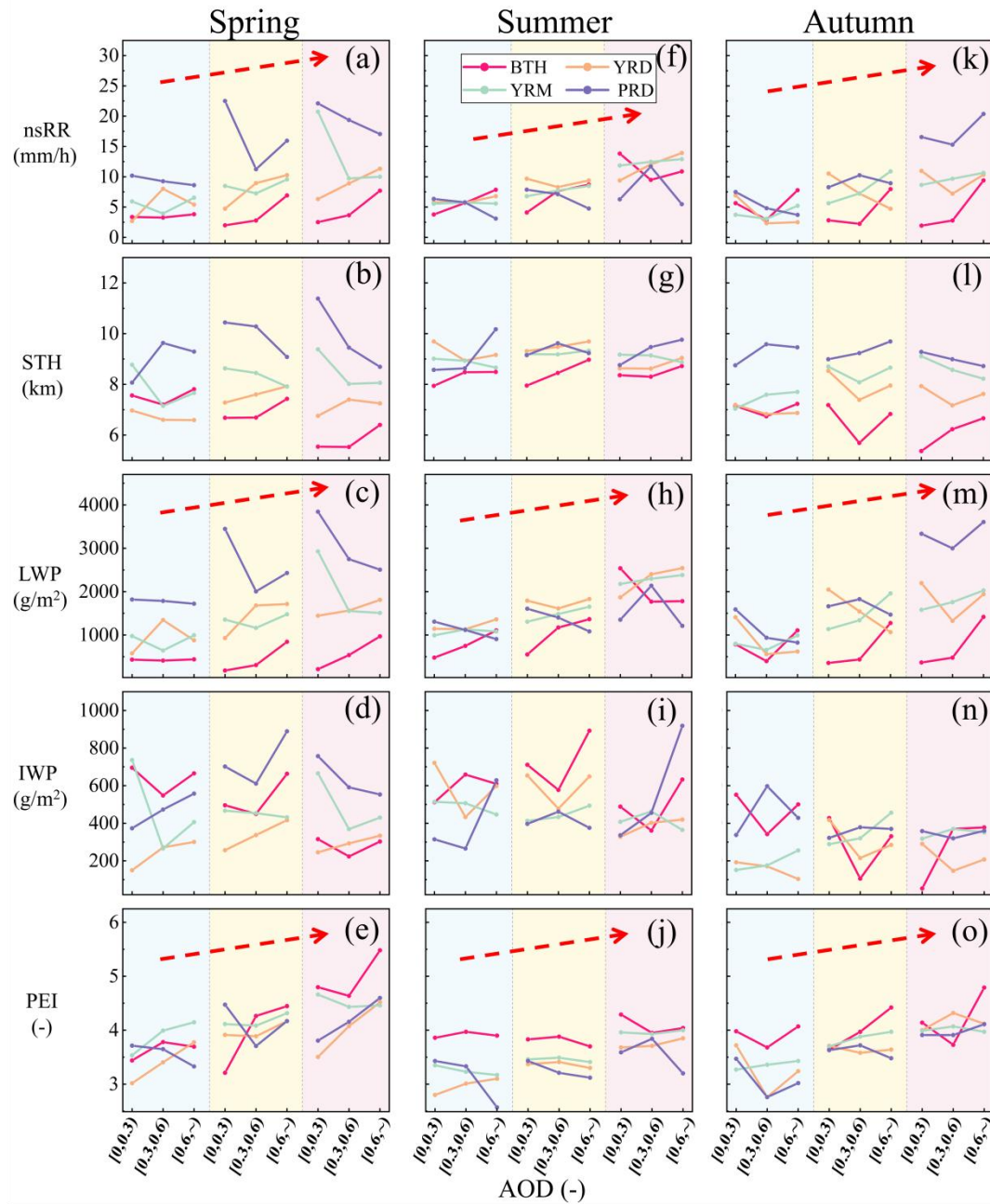
设置格式[phy]: 字体: (默认) Times New Roman, (中文)  
宋体, 小四

设置格式[phy]: 字体: (默认) Times New Roman, (中文)  
宋体, 小四

删除[phy]: Summer patterns (Fig. 6f–j) show modified the  
BTH responses under high RH; however, other regions remain  
consistent with prior trends in Fig. 3f–j

删除[phy]: .

删除[phy]: 6



561

562 **Fig. 7.** Point-line graphs of mean values for convective precipitation parameters

563 (nsRR, STH, LWP, IWP, and PEI) across seasons and regions. The analysis is based

564 on three AOD intervals and various RH conditions. Each subpanel displays RH

565 gradients from left to right: low RH (blue background), medium RH (yellow

566 background), and high RH (red background). The red dashed arrow represents the

567 overall variation trend of precipitation parameters with the increase of RH.

568 Fig. S6 presents point-line plots illustrating mean precipitation parameters associated

569 with stratiform precipitation. Increased RH consistently enhances these parameters,

删除[phy]: 6

设置格式[phy]: 字体颜色: 蓝色, 突出显示

570 particularly nsRR, LWP, and PEI, in BTH, YRD, and YRM. However, the PRD  
571 exhibits differing parameter responses across seasons under varying relative humidity  
572 conditions, similar to convective precipitation, as aerosol loading rises.

573 In addition to the thermodynamic conditions, CAPE was selected as a dynamic  
574 factor. Similar to the RH, the precipitation parameter characteristics across regions  
575 were investigated under varying CAPE conditions. As indicated by the red dashed  
576 arrows in Fig. 8, increasing CAPE values provide favorable dynamic conditions for  
577 convective precipitation, leading to rising STH, increased IWP, and enhanced  
578 ice-phase processes.

579 Spring (Fig. 8a–e) shows that in the PRD, the characteristics of nsRR, LWP, and  
580 PEI under varying AOD loading remain consistent across different CAPE conditions.

581 In contrast, the BTH, YRD, and YRM exhibit distinct variations in these parameters

582 under different CAPE levels. Summer (Fig. 8f–j) reveals that aerosol effects in the

583 BTH region demonstrate heightened sensitivity to CAPE variations. However, during

584 autumn convective precipitation (Fig. 8k–o), aerosols across the four regions exhibit

585 substantial sensitivity to CAPE, indicating different seasonal response mechanisms to

586 atmospheric instability in these areas.

587 Fig. S8 presents point-line plots of the mean precipitation parameters for

588 stratiform precipitation. Increasing CAPE enhances the STH and IWP parameters,

589 which is consistent with the convective precipitation patterns in Fig. 7.

删除[phy]: 7

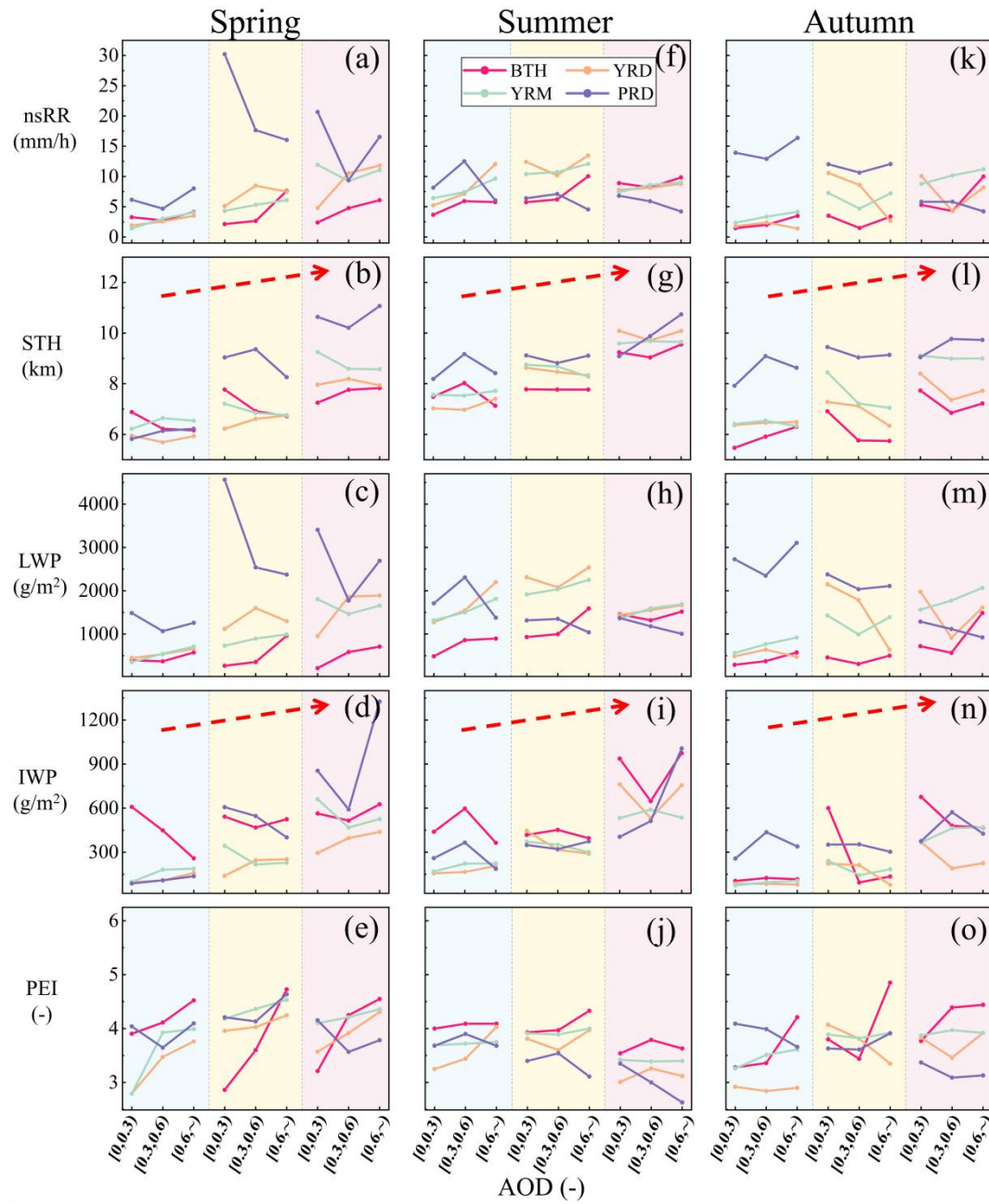
删除[phy]: 7

删除[phy]: 7

删除[phy]: 7

删除[phy]: 7

删除[phy]: 6



590

591 **Fig. 8.** Point-line graphs of mean values for convective precipitation parameters  
 592 across seasons and regions. The analysis is based on three AOD intervals and varying  
 593 CAPE scenarios. The form of this expression is similar to that shown in Fig. 6.

删除[phy]: 7

### 594 **5.2 Sensitivity of precipitation vertical profiles**

595 Furthermore, to examine aerosol sensitivity to thermodynamic conditions and  
 596 their effects on the vertical profiles of precipitation components, mean vertical  
 597 profiles of precipitation parameters ( $Z_e$ ,  $D_m$ ,  $N_w$ , RR) at varying RH levels are  
 598 illustrated, according to the technique shown in Fig. 4. Notably, as the parameter

删除[phy]: Sensitivity analysis of aerosols to meteorological factors in the vertical structure of precipitation

599 profile variations in Fig. 5 are concentrated within 0–10 km, the vertical coordinate  
600 range is limited to 0–10 km to emphasize the core precipitation processes. Moreover,  
601 where the curves intersect, dashed lines are employed to distinguish the selected  
602 profiles while maintaining the same representational integrity as the solid lines.

603 Spring convective precipitation (Fig. 9a–l) exhibits region-specific responses to  
604 RH, and in the BTH and YRD, increasing RH from low to medium ranges  
605 significantly elevates precipitation under high aerosol loading but suppresses it under  
606 medium loading (Fig. 9a). This discrepancy arises because abundant particles under  
607 elevated RH conditions undergo accelerated condensational growth, which increases  
608  $D_m$  (Fig. 9f). In contrast, the YRM and PRD show that RH enhancement primarily  
609 boosts precipitation, under low aerosol loading (blue curves). This is because in the  
610 YRD and YRM, particle competition continues to dominate at high loading, whereas  
611 added moisture at low loading facilitates condensational growth and enhances  $N_w$  (Fig.  
612 9g).

613 For the stratiform precipitation (Fig. 9m–x), the BTH, YRD, and YRM show  
614 consistent rightward shifts in RR curves across aerosol gradients as RH increases.  
615 This suggests that RH enhances moisture availability without modifying  
616 microphysical competition mechanisms. The PRD exhibits a response analogous to its  
617 convective precipitation feature.

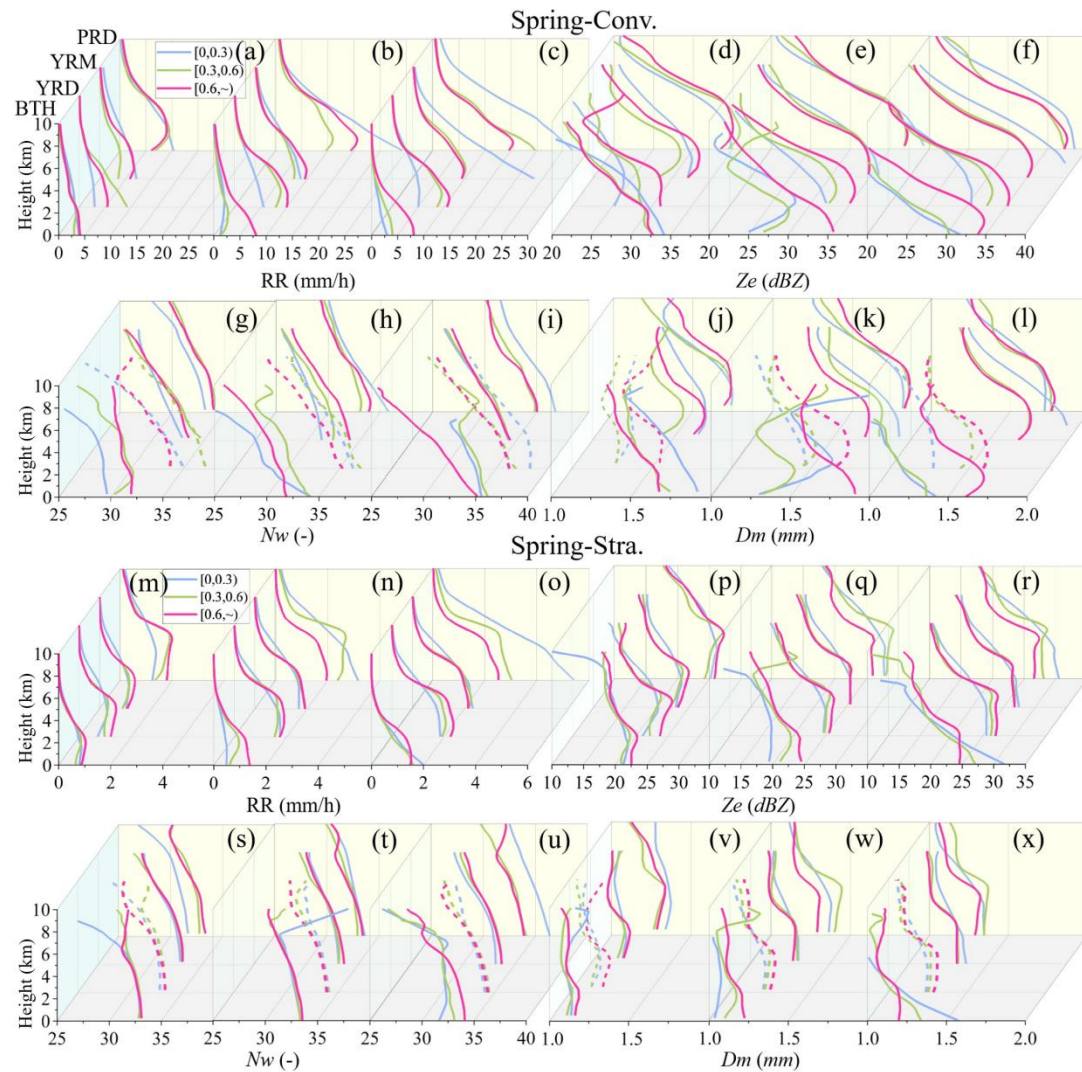
删除[phy]: 8

删除[phy]: 8

删除[phy]: 8

删除[phy]: 8

删除[phy]: 8



618

619 **Fig. 2.** Vertical profiles of mean precipitation parameters for convective (a–l) and  
 620 stratiform (m–x) precipitation in spring across four regions. The profiles are shown  
 621 under three AOD scenarios and RH conditions (arranged left to right as low, medium,  
 622 high RH; e.g., panels a–c correspond to low, medium, high RH, respectively). To  
 623 differentiate overlapping curves, selected profiles are plotted as dashed lines while  
 624 retaining the same representational validity as solid lines.

删除[phy]: 8

设置格式[phy]: 非突出显示

625 Additionally, similar characteristics are observed in convective and stratiform  
 626 precipitation during summer (Figs. S8) and autumn (Figs. S9) with variations in RH.  
 627 In general, increasing RH provides moisture conditions, accelerates cloud particle  
 628 condensational growth, and simultaneously increases both  $D_m$  and  $N_w$ , thereby  
 629 enhancing precipitation. However, this process also depends on the content of CCN  
 630 and various physical competition mechanisms.

设置格式[phy]: 突出显示

设置格式[phy]: 突出显示

631 Similarly, vertical profiles of precipitation parameters under varying CAPE  
632 conditions are presented. Fig. S10 illustrates consistent patterns between convective  
633 and stratiform precipitation during spring, echoing the fundamental characteristics in  
634 Fig. 8. This consistency suggests that RH and CAPE exert analogous influences on  
635 precipitation across aerosol loading gradients during spring.

设置格式[phy]: 突出显示

636 Summer convective precipitation (Fig. S11a–l) reveals distinct regional  
637 responses. In the BTH region, CAPE elevation significantly enhances low-AOD  
638 precipitation, likely driven by improved dynamic forcing that promotes cloud  
639 development (red point line in Fig. S7g). In contrast, the PRD exhibits pronounced  
640 precipitation suppression, most evident under moderate aerosol loading, where  
641 heightened CAPE intensifies particle break-up processes (Fig. S13h). These findings  
642 indicate that RH and CAPE exert divergent influences across regions. For RH,  
643 increasing moisture availability promotes particle growth via condensation under  
644 suited particle concentrations, but the Twomey effect dominates under high AOD  
645 loading, where particle competition for cloud water prevails. CAPE provides  
646 favorable dynamic conditions for cloud development, but simultaneously intensifies  
647 particle break-up through dynamic forces, which hinders the constant growth of cloud  
648 droplets and suppresses precipitation.

设置格式[phy]: 突出显示

设置格式[phy]: 突出显示

设置格式[phy]: 突出显示

### 649 **5.3 Sensitivity of precipitation microphysical processes**

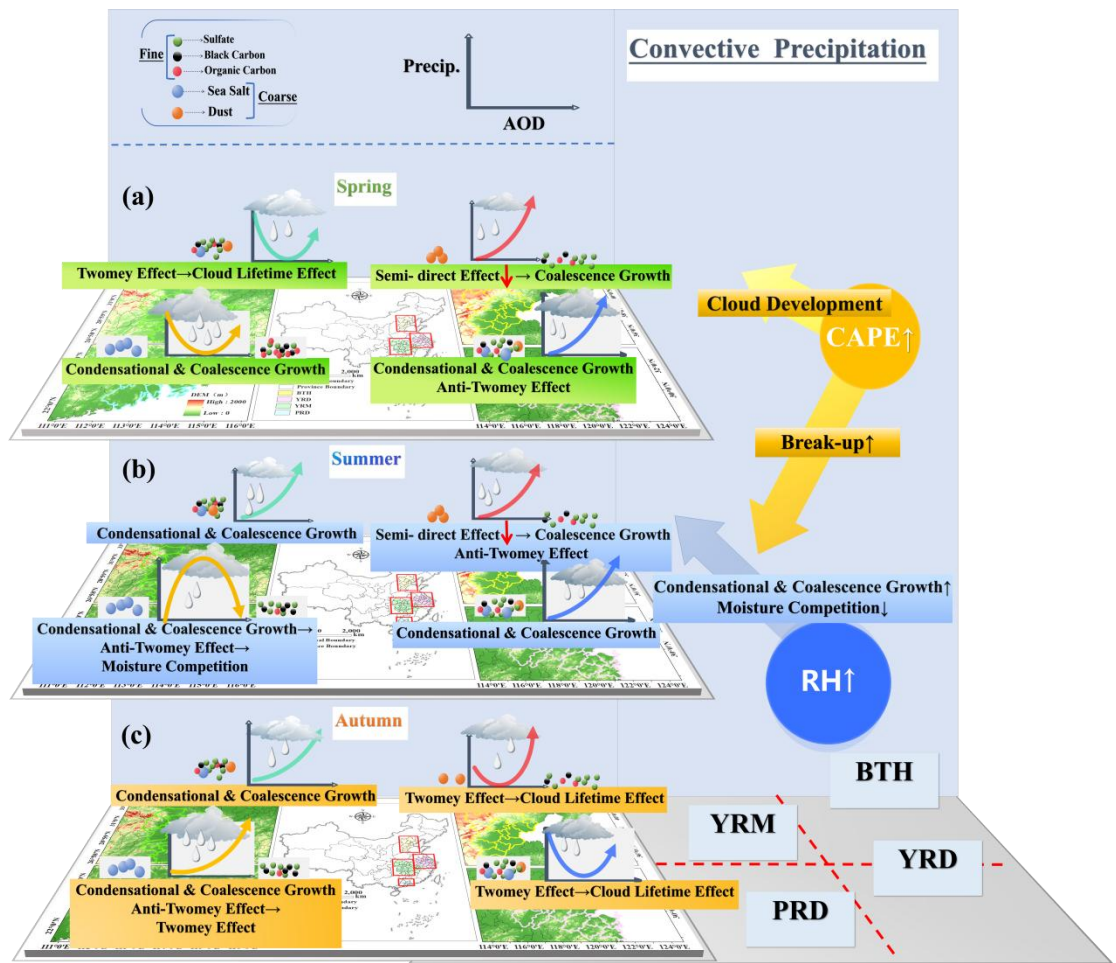
删除[phy]: *Sensitivity analysis of aerosols to meteorological factors in precipitation*

650 To validate the aforementioned inferences, the proportions of break-up and  
651 coalescence processes in convective and stratiform precipitation are further  
652 investigated. Fig. S13 reveals that in convective precipitation, an increase in RH  
653 generally correlates with enhanced coalescence (white-green bars in the upper half;  
654 the trend is shown by the blue arrows) and reduced break-up (white-green bars in the  
655 lower half). Conversely, increasing CAPE is associated with decreased coalescence  
656 (green line in the upper half) and intensified break-up (yellow line in the lower half;  
657 the trend is shown by the red arrows), particularly in summer and the PRD region. As  
658 illustrated in Fig. S14, stratiform precipitation demonstrates similarities to convective  
659 precipitation, and the increase in RH makes the enhancement of coalescence

设置格式[phy]: 突出显示

设置格式[phy]: 突出显示

660 processes more universal.



661

662 **Fig. 10.** Theoretical framework of aerosol impact on convective precipitation in the

663 BTH, YRD, YRM, and PRD: (a) spring, (b) summer, and (c) autumn. Symbol

664 conventions, ↑: Enhancement of process; ↓: Weakening of process; →: Transition

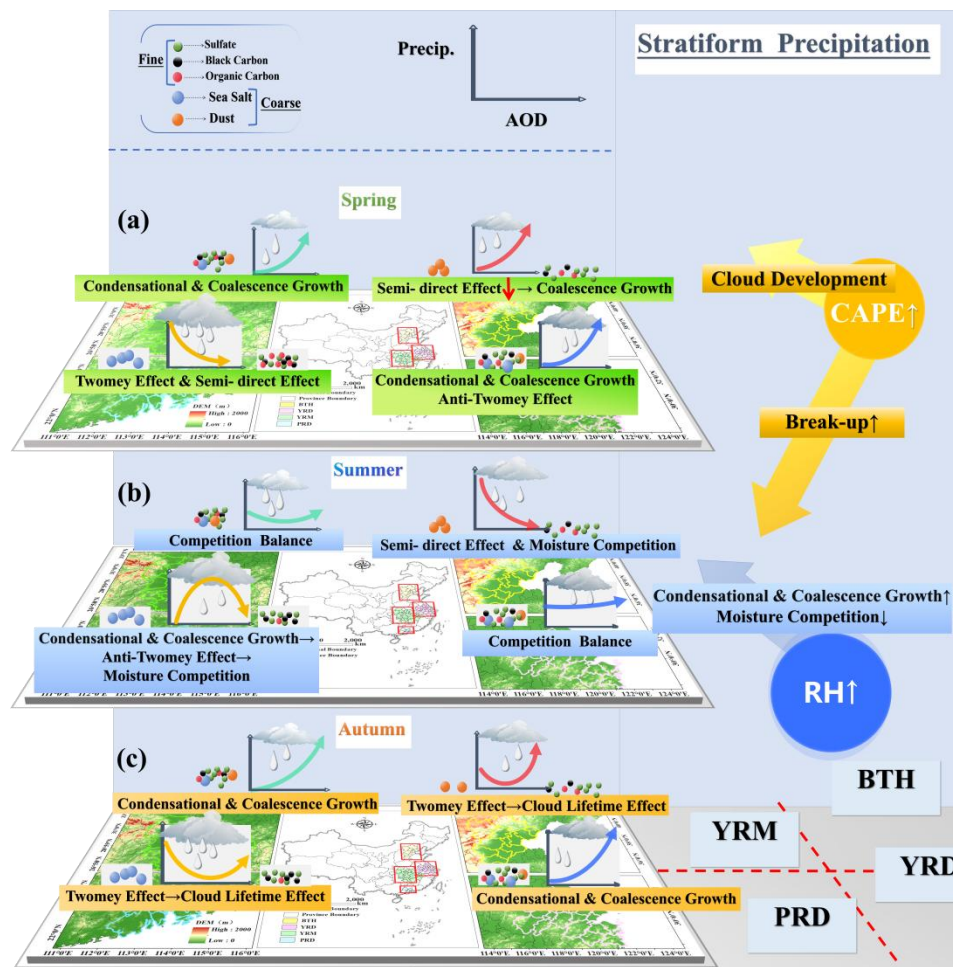
665 from left-side process dominance to right-side process dominance; Right-side CAPE

666 arrows: ↗ promotes precipitation; ↘ suppresses precipitation; Right-side RH arrows:

667 ↗ enhances precipitation processes. Arrow length reflects the relative process

668 intensity.

删除[phy]: 9



669

670 **Fig. 11.** Theoretical framework of aerosol impact on stratiform precipitation in the  
 671 BTH, YRD, YRM, and PRD. The form of this expression is similar to that shown in  
 672 Fig. 9.

删除[phy]: 0

## 673 **6 Conclusions**

674 This study systematically examined the impact of aerosols on precipitation  
 675 parameters, vertical profiles, and microphysical processes in convective and  
 676 stratiform precipitation across China's four major urban clusters (the BTH, YRD,  
 677 YRM, and PRD) — during spring, summer, and autumn, utilizing the  
 678 DPR-MERRA-2-ERA5 dataset. It further explores aerosol sensitivity to RH and  
 679 CAPE, revealing regional heterogeneity, seasonal dependency, and the underlying  
 680 microphysical processes of aerosol effects. The research indicates that physical  
 681 processes, including condensational growth, coalescence growth, semi-direct effects,  
 682 and moisture competition effects from aerosol-sourced CCN, trigger the Twomey

删除[phy]: vertical structures

683 effect, Anti-Twomey effect, and cloud lifetime effect, resulting in varied precipitation  
684 alterations. Additionally, an increase in aerosol loading diminishes the regional  
685 disparities in precipitation characteristics, with a more pronounced effect during the  
686 spring and summer. The precipitation parameters exhibit greater regional variability  
687 than seasonal variability, and convective precipitation experiences more significant  
688 seasonal and regional changes compared to stratiform precipitation. Based on the  
689 findings in Section 3-5, the physical mechanisms by which aerosols at varying  
690 concentrations influence convective precipitation (Fig. 10) and stratiform  
691 precipitation (Fig. 11) are illustrated, with the following specific conclusions:

692 For convective precipitation (Fig. 10): Precipitation in the BTH region is  
693 influenced by seasonal variations in dust aerosols. During spring (Fig. 10a) and  
694 summer (Fig. 10b), dust aerosols exert significant impacts, whereas their  
695 contributions declines in autumn (Fig. 10c), resulting in distinct precipitation  
696 characteristics. Specifically, DUA play a dual role: it suppresses precipitation through  
697 the semi-direct effect (by evaporating cloud droplets), yet also invigorates deep  
698 convection by serving as efficient IN. This competitive dynamic between the  
699 suppression of warm-rain processes and the invigoration of cold-rain processes is  
700 central to the complex aerosol-precipitation relationship. In autumn, when the DUA  
701 constitutes a minor fraction, rising aerosol loadings initially suppress precipitation  
702 through the Twomey effect, while simultaneously promoting cloud development,  
703 subsequently enhancing precipitation through increased CCN availability. The YRD  
704 exhibits a persistent precipitation increase with increasing aerosol loadings owing to  
705 the ample moisture supply. While sharing similar seasonal trends with the BTH, its  
706 underlying mechanisms differ significantly: abundant water vapor enables continuous  
707 precipitation growth during spring (Fig. 10a) and summer (Fig. 10b), primarily  
708 attributable to enhanced droplet condensation and coalescence processes. The PRD  
709 exhibits the most pronounced seasonal variability, attributable to shifts in the  
710 composition of hygroscopic aerosols (SSA). During spring (Fig. 10a), precipitation in  
711 the PRD is significantly higher than in other regions under low aerosol loading due to  
712 SSAs. As aerosol loadings increase, diminishing SSA proportion weakens this

删除[phy]: 9

删除[phy]: 0

删除[phy]: 9

删除[phy]: 9

删除[phy]: 9

删除[phy]: 9

设置格式[phy]: 字体: (默认) Times New Roman, (中文)  
宋体, 小四

设置格式[phy]: 字体: (默认) Times New Roman, (中文)  
宋体, 小四

设置格式[phy]: 字体: (默认) Times New Roman, (中文)  
宋体, 小四

设置格式[phy]: 字体: (默认) Times New Roman, (中文)  
宋体, 小四

设置格式[phy]: 字体: (默认) Times New Roman, (中文)  
宋体, 小四

删除[phy]: Specifically, as the total aerosol loading increases, the proportion of dust aerosols rapidly decrease. This reduction weakens the semi-direct effect of dust while enhancing the particle coalescence processes, thereby enhancing precipitation. However, insufficient moisture supply and frequent dust events in spring collectively reduce the overall precipitation below the levels observed in the other three regions.

删除[phy]: 9

删除[phy]: 9

删除[phy]: 9

713 enhancement until rising hygroscopic organic carbon subsequently reinforces  
714 precipitation. In summer (Fig. 10b), sufficient moisture initially promotes droplet  
715 growth through condensation-coalescence under low aerosol loadings. However, the  
716 subsequent aerosol accumulation intensifies moisture competition and suppresses  
717 precipitation. Monsoon-influenced sea-salt overabundance (Xiao et al., 2025) further  
718 amplifies this competition effect, resulting in overall lower precipitation rates  
719 compared to other regions.

720 For stratiform precipitation (Fig. 11): Overall, stratiform and convective  
721 precipitation share fundamental similarities yet exhibit distinct microphysical  
722 processes due to differing cloud formation conditions. With a lower moisture supply  
723 than convective systems, stratiform precipitation in the BTH region is suppressed  
724 during summer (Fig. 11b) through aerosol semi-direct effects and moisture  
725 competition. Similarly, in the PRD, spring precipitation is reduced by organic carbon  
726 aerosols (Fig. 11a), which act as both hygroscopic and light-absorbing particles  
727 (Zhuang et al., 2025). This occurs when an insufficient moisture supply enhances the  
728 radiation-absorbing effect, dominating the precipitation reduction mechanism.

729 Furthermore, variations in RH and CAPE modulate aerosol-precipitation  
730 interactions, as shown in Figs. 10–11. Specifically, elevated RH indicates enhanced  
731 moisture availability, which facilitates rapid droplet growth through condensation and  
732 coalescence under suitable aerosol loading. Regarding dynamic influences, increased  
733 CAPE provides favorable conditions for cloud development while simultaneously  
734 enhancing droplet break-up through intensified turbulence, hindering cloud droplet  
735 growth, and suppressing precipitation, particularly in summer and the PRD region.

736 Overall, aerosol impacts on precipitation result from complex couplings among  
737 regional aerosol composition, moisture transport patterns, atmospheric stability, and  
738 precipitation types, generating both linear and nonlinear responses. These complex  
739 dynamics establish essential theoretical underpinnings for formulating atmospheric  
740 cleanup techniques in significant metropolitan centers, enhancing early warning  
741 systems for extreme precipitation occurrences, and refining regional climate models.

742 **7 Discussion**

743 Building on the findings of (Peng et al., 2025), which investigated the effects of  
744 fine and coarse aerosols on summer precipitation structure and microphysics in the  
745 YRD region, the present study expands the scope of analysis to examine aerosol  
746 impacts on precipitation vertical profiles and microphysical processes across multiple  
747 regions and seasons in China. This expanded scope, combined with a unified  
748 analytical methodology, enables a systematic cross-regional and cross-seasonal  
749 comparison that mitigates inconsistencies often associated with disparate data sources  
750 or methods, yielding the following key findings: (1)Enhanced aerosol loading reduces  
751 regional precipitation disparities, most pronounced in spring and summer.  
752 (2)Precipitation exhibits stronger regional than seasonal variability. (3)The BTH  
753 precipitation is dominated by dust aerosols, whereas the YRD and PRD are influenced  
754 by sea salt aerosols. These conclusions are primarily derived from analyses of  
755 satellite-based datasets, which provide extensive spatial coverage, high spatiotemporal  
756 resolution, and continuous temporal monitoring.

757 The results provide further evidence for several established mechanisms: The  
758 dominant role of dust aerosols in the BTH region aligns with existing research (Xi et  
759 al., 2024; Xiao et al., 2025). manifesting as impacts on precipitation through ARI  
760 (Sun and Zhao, 2021) and semi-direct effects, and also serving as effective IN to  
761 promote convective cloud development (Xi et al., 2025). Furthermore, the  
762 precipitation-enhancing effect of sea salt aerosols in the PRD region is consistent with  
763 prior observations (Chen et al., 2025; Guo et al., 2022).

764 However, as noted by Stier et al. (2024) and Zhao et al. (2024), aerosol impacts  
765 on precipitation remain highly complex, and their net effects are still subject to  
766 considerable uncertainty across different scales. Multiple factors are known to  
767 modulate precipitation processes, such as vertical wind shear (Riemer et al., 2010).  
768 cloud properties (Shao and Liu, 2005; Zhao et al., 2012), and latent heating (Zhu et al.,  
769 2025). Therefore, a critical challenge for future research lies in better disentangling

删除[phy]: vertical structures

设置格式[phy]: 字体: (中文) 宋体, (中文) 中文(简体)

设置格式[phy]: 字体: (中文) Times New Roman

设置格式[phy]: (中文) 中文(简体)

设置格式[phy]: 字体: (中文) Times New Roman

设置格式[phy]: (中文) 中文(简体)

删除[p hy]: (

删除[p hy]: ,

删除[p hy]: ;

删除[p hy]: ,

设置格式[phy]: (中文) 中文(简体)

设置格式[phy]: (中文) 中文(简体)

设置格式[phy]: (中文) 中文(简体)

设置格式[phy]: (中文) 中文(简体)

770 the influence of such environmental meteorological factors from the overall aerosol  
771 effect.

772 In addition, it is important to acknowledge that considerable uncertainties  
773 persist in satellite data processing and retrieval algorithms, especially under complex  
774 atmospheric and surface conditions. Additionally, spatiotemporal resolution and  
775 format discrepancies across multisource data introduce unavoidable uncertainties.  
776 This study primarily focuses on the vertical structural characteristics of precipitation,  
777 whereas the analysis of aerosol data lacks comprehensive three-dimensional matching.  
778 Currently, vertical profiling of aerosols relies primarily on aircraft sounding (Zhou et  
779 al., 2023) and simulated radar signals (Fajardo-Zambrano et al., 2022), which remain  
780 spatially limited. Satellite remote sensing is hindered by inadequate resolution and  
781 deficiency in three-dimensional information (Li et al., 2022). However, the successful  
782 launch and stable operation of EarthCARE now facilitates accurate three-dimensional  
783 vertical profiling of clouds and aerosols via lidar (ATLID) and cloud profiling radar  
784 (CPR) (Irbah et al., 2023). The integration of high-precision vertical profiles from  
785 ATLID (aerosols), CPR (clouds), and GPM DPR (precipitation) will enable future  
786 researchers to quantify how aerosol layers at different altitudes modulate cloud  
787 microphysics and precipitation formation (Li et al., 2025b). For instance, this  
788 multi-source dataset provides an unprecedented opportunity to systematically unravel  
789 the distinct roles aerosols play in the microphysics of different hydrometeor phases,  
790 including the ice layer, melting layer, and liquid layer. This layered investigation will  
791 provide a clear path toward the mechanistic understanding of aerosol impacts on  
792 precipitation evolution, thereby addressing a critical gap stemming from insufficient  
793 3D aerosol-cloud-precipitation co-location. Additionally, a more complete  
794 understanding of aerosol-precipitation interactions must account for the complex  
795 synergies among environmental factors, leveraging advanced statistical or modeling  
796 methods in a multi-factor analytical framework. Notably, as Zhao et al.( 2025)  
797 revealed distinct aerosol-cloud interaction patterns over land versus ocean in the YRD,  
798 the absence of cloud parameter products in this study may inherently limit the depth

删除[phy]: Nevertheless

设置格式[phy]: 字体: (中文) 宋体, 突出显示, (中文) 中文(简体)

设置格式[phy]: 字体: (中文) 宋体, (中文) 中文(简体)

设置格式[phy]: 字体: (中文) 宋体, (中文) 中文(简体)

设置格式[phy]: 字体: (中文) 宋体, (中文) 中文(简体)

删除[phy]: **Future collaborative observations from the GPM and EarthCARE will produce enhanced datasets on clouds, precipitation, and aerosols, thus facilitating more robust in-depth studies within this research framework.**

设置格式[phy]: 字体: (中文) 宋体, 突出显示, (中文) 中文(简体)

删除[phy]: Subsequent research should integrate supplementary meteorological variables and machine-learning methodologies to more effectively delineate aerosol effects and examine their responsiveness to meteorological influences.

799 of the aerosol-precipitation mechanism analysis. This methodological constraint thus  
800 necessitates the future integration of high-resolution cloud parameter datasets to refine  
801 research findings, enabling a comprehensive exploration of  
802 aerosol-cloud-precipitation coupling mechanisms, specifically encompassing dry and  
803 wet aerosol removal processes and precipitation feedback loops.

#### 804 **Data availability**

805 The V07A GPM 2ADPR products used in this paper are openly available at the  
806 NASA Goddard Space Flight Center's Precipitation Processing System (PPS) team  
807 (<https://storm.pps.eosdis.nasa.gov/storm/>). [MERRA-2 data can be downloaded from https://gmao.gsfc.nasa.gov/reanalysis/MERRA-2/data\\_access/](https://gmao.gsfc.nasa.gov/reanalysis/MERRA-2/data_access/). The ERA5 data can  
808 [be downloaded from https://www.ecmef.](https://www.ecmef.int/en/forecasts/dataset/ecmwf-reanalysis-v5)  
809 [https://www.ecmef.](https://www.ecmef.int/en/forecasts/dataset/ecmwf-reanalysis-v5)  
810 [int/en/forecasts/dataset/ecmwf-reanalysis-v5](https://www.ecmef.int/en/forecasts/dataset/ecmwf-reanalysis-v5).

#### 811 **Author contributions**

812 H P & Z L: Writing – review & editing, Writing – original draft, Visualization,  
813 Validation, Methodology, Investigation. X H: Writing – original draft, Validation,  
814 Supervision, Software, Resources, Methodology, Investigation, Formal analysis, Data  
815 curation, Conceptualization. W A: Writing – review & editing, Project administration.  
816 S H & J Q: Writing – review & editing, Investigation. X Z: Writing – review &  
817 editing, Funding acquisition, Formal analysis.

#### 818 **Declaration of competing interest**

819 The authors declare that they have no known competing financial interests or  
820 personal relationships that could have appeared to influence the work reported in this  
821 paper.

#### 822 **Acknowledgments**

823 Z<sub>v</sub> Li and H<sub>v</sub> P<sub>v</sub> contributed equally to this work and should be considered as  
824 co-first authors. The authors thank the anonymous reviewers for their constructive  
825 comments and suggestions, which have greatly improved the quality of this paper.

删除[phy]: hen

删除[phy]: eyuan

删除[phy]: eng

#### 826 **Financial support**

827 This work has been jointly supported by the National Natural Science  
828 Foundation of China (grant nos. 42305150).

829

## 830 **References**

- 831 Ackerman, A. S., Toon, O. B., Stevens, D. E., Heymsfield, A. J., Ramanathan, V., and Welton, E. J.:  
832 Reduction of Tropical Cloudiness by Soot, *Science*, Vol.288, 1042–1047,  
833 <https://doi.org/10.1126/science.288.5468.1042>, 2000.
- 834 Albrecht, B. A.: Aerosols, Cloud Microphysics, and Fractional Cloudiness, *Science*, 245,  
835 1227–1230, <https://doi.org/10.1126/science.245.4923.1227>, 1989.
- 836 Buchard, V., Randles, C. A., Da Silva, A. M., Darmenov, A., Colarco, P. R., Govindaraju, R.,  
837 Ferrare, R., Hair, J., Beyersdorf, A. J., Ziemba, L. D., and Yu, H.: The MERRA-2 aerosol  
838 reanalysis, 1980 onward. Part II: Evaluation and case studies, *J. Climate*, 30, 6851–6872,  
839 <https://doi.org/10.1175/JCLI-D-16-0613.1>, 2017.
- 840 Chandrasekar, V. and Le, M.: Evaluation of profile classification module of GPM-DPR algorithm  
841 after launch, in: 2015 IEEE International Geoscience and Remote Sensing Symposium  
842 (IGARSS), IGARSS 2015 - 2015 IEEE International Geoscience and Remote Sensing  
843 Symposium, Milan, Italy, 5174–5177, <https://doi.org/10.1109/igarss.2015.7326999>, 2015.
- 844 Chang, D., Cheng, Y., Reutter, P., Trentmann, J., Burrows, S. M., Spichtinger, P., Nordmann, S.,  
845 Andreae, M. O., Pöschl, U., and Su, H.: Comprehensive mapping and characteristic regimes  
846 of aerosol effects on the formation and evolution of pyro-convective clouds, *Atmos. Chem.*  
847 *Phys.*, 15, 10325–10348, <https://doi.org/10.5194/acp-15-10325-2015>, 2015.
- 848 Chen, F., Yang, Y., Yu, L., Li, Y., Liu, W., Liu, Y., and Lolli, S.: Distinct effects of fine and coarse  
849 aerosols on microphysical processes of shallow-precipitation systems in summer over  
850 southern China, *Atmos. Chem. Phys.*, 25, 1587–1601,  
851 <https://doi.org/10.5194/acp-25-1587-2025>, 2025.
- 852 Chen, Y. and Luo, Y.: Analysis of Paths and Sources of Moisture for the South China Rainfall  
853 during the Presummer Rainy Season of 1979–2014, *J Meteorol Res*, 32, 744–757,  
854 <https://doi.org/10.1007/s13351-018-8069-7>, 2018.
- 855 Day, J. A., Fung, I., and Liu, W.: Changing character of rainfall in eastern China, 1951–2007,  
856 *Proceedings of the National Academy of Sciences*, 115, 2016–2021,  
857 <https://doi.org/10.1073/pnas.1715386115>, 2018.
- 858 Dong, X., Li, R., Wang, Y., Fu, Y., and Zhao, C.: Potential impacts of sahara dust aerosol on  
859 rainfall vertical structure over the atlantic ocean as identified from EOF analysis, *JGR*  
860 *Atmospheres*, 123, 8850–8868, <https://doi.org/10.1029/2018JD028500>, 2018.
- 861 Fajardo-Zambrano, C. M., Bravo-Aranda, J. A., Granados-Muñoz, M. J., Montilla-Rosero, E.,  
862 Casquero-Vera, J. A., Rejano, F., Castillo, S., and Alados-Arboledas, L.: Lidar and Radar  
863 Signal Simulation: Stability Assessment of the Aerosol–Cloud Interaction Index, *Remote*  
864 *Sensing*, 14, 1333, <https://doi.org/10.3390/rs14061333>, 2022.
- 865 Fan, J., Zhang, R., Li, G., and Tao, W.: Effects of aerosols and relative humidity on cumulus  
866 clouds, *J. Geophys. Res.*, 112, <https://doi.org/10.1029/2006jd008136>, 2007.
- 867 Garrett, T. J. and Zhao, C.: Increased Arctic cloud longwave emissivity associated with pollution

868 from mid-latitudes, *Nature*, 440, 787–789, <https://doi.org/10.1038/nature04636>, 2006.

869 Gettelman, A.: Putting the clouds back in aerosol–cloud interactions, *Atmos. Chem. Phys.*, 15,  
870 12397–12411, <https://doi.org/10.5194/acp-15-12397-2015>, 2015.

871 Guo, J., Su, T., Li, Z., Miao, Y., Li, J., Liu, H., Xu, H., Cribb, M., and Zhai, P.: Declining  
872 frequency of summertime local-scale precipitation over eastern China from 1970 to 2010 and  
873 its potential link to aerosols, *Geophysical Research Letters*, 44, 5700–5708,  
874 <https://doi.org/10.1002/2017GL073533>, 2017.

875 Guo, J., Liu, H., Li, Z., Rosenfeld, D., Jiang, M., Xu, W., Jiang, J. H., He, J., Chen, D., Min, M.,  
876 and Zhai, P.: Aerosol-induced changes in the vertical structure of precipitation: a perspective  
877 of TRMM precipitation radar, *Atmos. Chem. Phys.*, 18, 13329–13343,  
878 <https://doi.org/10.5194/acp-18-13329-2018>, 2018.

879 Guo, J., Su, T., Chen, D., Wang, J., Li, Z., Lv, Y., Guo, X., Liu, H., Cribb, M., and Zhai, P.:  
880 Declining Summertime Local-Scale Precipitation Frequency Over China and the United  
881 States, 1981–2012: The Disparate Roles of Aerosols, *Geophysical Research Letters*, 46,  
882 13281–13289, <https://doi.org/10.1029/2019GL085442>, 2019.

883 Guo, J., Luo, Y., Yang, J., Furtado, K., and Lei, H.: Effects of anthropogenic and sea salt aerosols  
884 on a heavy rainfall event during the early-summer rainy season over coastal Southern China,  
885 *Atmospheric Research*, 265, 105923, <https://doi.org/10.1016/j.atmosres.2021.105923>, 2022.

886 Hersbach, H., Bell, B., Berrisford, P., Hirahara, S., Horányi, A., Muñoz-Sabater, J., Nicolas, J.,  
887 Peubey, C., Radu, R., Schepers, D., Simmons, A., Soci, C., Abdalla, S., Abellan, X., Balsamo,  
888 G., Bechtold, P., Biavati, G., Bidlot, J., Bonavita, M., De Chiara, G., Dahlgren, P., Dee, D.,  
889 Diamantakis, M., Dragani, R., Flemming, J., Forbes, R., Fuentes, M., Geer, A., Haimberger,  
890 L., Healy, S., Hogan, R. J., Hólm, E., Janisková, M., Keeley, S., Laloyaux, P., Lopez, P., Lupu,  
891 C., Radnoti, G., De Rosnay, P., Rozum, I., Vamborg, F., Villaume, S., and Thépaut, J.: The  
892 ERA5 global reanalysis, *Quart J Royal Meteor Soc*, 146, 1999–2049,  
893 <https://doi.org/10.1002/qj.3803>, 2020.

894 Hou, A. Y., Kakar, R. K., Neeck, S., Azarbarzin, A. A., Kummerow, C. D., Kojima, M., Oki, R.,  
895 Nakamura, K., and Iguchi, T.: The Global Precipitation Measurement Mission, *Bull. Amer.*  
896 *Meteor. Soc.*, 95, 701–722, <https://doi.org/10.1175/bams-d-13-00164.1>, 2014.

897 Hu, X., Ai, W., Qiao, J., Hu, S., Han, D., and Yan, W.: Microphysics of Summer Precipitation  
898 Over Yangtze-Huai River Valley Region in China Revealed by GPM DPR Observation, *Earth*  
899 *and Space Science*, 9, <https://doi.org/10.1029/2021ea002021>, 2022.

900 Hu, X., Ai, W., Qiao, J., and Yan, W.: Insight into global climatology of melting layer: Latitudinal  
901 dependence and orographic relief, *Theor Appl Climatol*, 155, 4863–4873,  
902 <https://doi.org/10.1007/s00704-024-04926-6>, 2024.

903 Huang, J., Wang, T., Wang, W., Li, Z., and Yan, H.: Climate effects of dust aerosols over East  
904 Asian arid and semiarid regions, *JGR Atmospheres*, 119,  
905 <https://doi.org/10.1002/2014jd021796>, 2014.

906 IPCC. 2013. Climate Change 2013: The Physical Science Basis. Contribution of Working Group I  
907 to the Fifth Assessment Report of the Intergovernmental Panel on Climate Change  
908 [M].Stocker TF,QinD, PlattnerG K, et al.,Eds.Cambridge, United Kingdom and New York,  
909 NY, USA: Cambridge UniversityPress, 1535pp.

910 IPCC. 2021. Climate Change 2021: The Physical Science Basis. Contribution of Working Group I  
911 to theSixth Assessment Report of the Intergovernmental Panel on Climate Change

912 [M].Masson-DelmotteV, ZhaiP, PiraniA, et al.,Eds.Cambridge, United Kingdom and New  
913 York, NY, USA: Cambridge University Press, 2338pp.

914 Irbah, A., Delanoë, J., Van Zadelhoff, G.-J., Donovan, D. P., Kollias, P., Puigdomènech Treserras,  
915 B., Mason, S., Hogan, R. J., and Tatarevic, A.: The classification of atmospheric  
916 hydrometeors and aerosols from the EarthCARE radar and lidar: the A-TC, C-TC and AC-TC  
917 products, *Atmos. Meas. Tech.*, 16, 2795–2820, <https://doi.org/10.5194/amt-16-2795-2023>,  
918 2023.

919 Ji, Z. and Tian, S.: A novel potential cause of extreme precipitation in the northwest China,  
920 *Heliyon*, 10, e30826, <https://doi.org/10.1016/j.heliyon.2024.e30826>, 2024.

921 Jiang, M., Li, Y., Hu, W., Yang, Y., Brasseur, G., and Zhao, X.: Model-based insights into aerosol  
922 perturbation on pristine continental convective precipitation, *Atmos. Chem. Phys.*, 23,  
923 4545–4557, <https://doi.org/10.5194/acp-23-4545-2023>, 2023.

924 Kotsuki, S., Terasaki, K., Satoh, M., and Miyoshi, T.: Ensemble-based data assimilation of GPM  
925 DPR reflectivity: Cloud microphysics parameter estimation with the nonhydrostatic  
926 icosahedral atmospheric model (NICAM), *Journal of Geophysical Research: Atmospheres*,  
927 128, <https://doi.org/10.1029/2022jd037447>, 2023.

928 Kumjian, M. R. and Prat, O. P.: The Impact of Raindrop Collisional Processes on the Polarimetric  
929 Radar Variables, *Journal of the Atmospheric Sciences*, 71, 3052–3067,  
930 <https://doi.org/10.1175/jas-d-13-0357.1>, 2014.

931 Lasser, M., O, S., and Foelsche, U.: Evaluation of GPM-DPR precipitation estimates with  
932 WegenerNet gauge data, *Atmos. Meas. Tech.*, 12, 5055–5070,  
933 <https://doi.org/10.5194/amt-12-5055-2019>, 2019.

934 Lee, S. S., Donner, L. J., Phillips, V. T. J., and Ming, Y.: The dependence of aerosol effects on  
935 clouds and precipitation on cloud-system organization, shear and stability, *Journal of*  
936 *Geophysical Research: Atmospheres*, 113, <https://doi.org/10.1029/2007JD009224>, 2008.

937 Li, J., Carlson, B. E., Yung, Y. L., Lv, D., Hansen, J., Penner, J. E., Liao, H., Ramaswamy, V.,  
938 Kahn, R. A., Zhang, P., Dubovik, O., Ding, A., Lacis, A. A., Zhang, L., and Dong, Y.:  
939 Scattering and absorbing aerosols in the climate system, *Nat Rev Earth Environ*, 3, 363–379,  
940 <https://doi.org/10.1038/s43017-022-00296-7>, 2022.

941 Li, J., Zhao, C., Sun, Y., Zhao, X., Yang, J., Yang, Y., Chen, A., and Zhou, Y.: Distinct Aerosol  
942 Impacts on Local Scale Convective Rainfall Between Sichuan Basin and North China Plain  
943 Regions in China, *Journal of Geophysical Research: Atmospheres*, 130, e2024JD042649,  
944 <https://doi.org/10.1029/2024JD042649>, 2025a.

945 Li, Z., Lau, W. K.-M., Ramanathan, V., Wu, G., Ding, Y., Manoj, M. G., Liu, J., Qian, Y., Li, J.,  
946 Zhou, T., Fan, J., Rosenfeld, D., Ming, Y., Wang, Y., Huang, J., Wang, B., Xu, X., Lee, S.-S.,  
947 Cribb, M., Zhang, F., Yang, X., Zhao, C., Takemura, T., Wang, K., Xia, X., Yin, Y., Zhang, H.,  
948 Guo, J., Zhai, P. M., Sugimoto, N., Babu, S. S., and Brasseur, G. P.: Aerosol and monsoon  
949 climate interactions over asia, *Reviews of Geophysics*, 54, 866–929,  
950 <https://doi.org/10.1002/2015RG000500>, 2016.

951 Li, Z., Wang, Y., Guo, J., Zhao, C., Cribb, M. C., Dong, X., Fan, J., Gong, D., Huang, J., Jiang, M.,  
952 Jiang, Y., Lee, S.-S., Li, H., Li, J., Liu, J., Qian, Y., Rosenfeld, D., Shan, S., Sun, Y., Wang, H.,  
953 Xin, J., Yan, X., Yang, X., Yang, X., Zhang, F., and Zheng, Y.: East asian study of  
954 tropospheric aerosols and their impact on regional clouds, precipitation, and climate  
955 (EAST-AIRCPC), *Journal of Geophysical Research: Atmospheres*, 124, 13026–13054,

956 <https://doi.org/10.1029/2019JD030758>, 2019.

957 Li, Z., Ge, S., Hu, X., Ai, W., Tang, J., Qiao, J., Hu, S., Zhao, X., Wu, H., Li, Z., Ge, S., Hu, X., Ai,  
958 W., Tang, J., Qiao, J., Hu, S., Zhao, X., and Wu, H.: Preliminary analysis of a novel  
959 spaceborne pseudo tripe-frequency radar observations on cloud and precipitation:  
960 EarthCARE CPR-GPM DPR coincidence dataset, *Remote Sens.*, 17,  
961 <https://doi.org/10.3390/rs17152550>, 2025b.

962 Liu, C. and Zipser, E. J.: The global distribution of largest, deepest, and most intense precipitation  
963 systems, *Geophysical Research Letters*, 42, 3591–3595,  
964 <https://doi.org/10.1002/2015gl063776>, 2015.

965 Liu, Y., De Leeuw, G., Kerminen, V.-M., Zhang, J., Zhou, P., Nie, W., Qi, X., Hong, J., Wang, Y.,  
966 Ding, A., Guo, H., Krüger, O., Kulmala, M., and Petäjä, T.: Analysis of aerosol effects on  
967 warm clouds over the Yangtze River Delta from multi-sensor satellite observations, *Atmos.*  
968 *Chem. Phys.*, 17, 5623–5641, <https://doi.org/10.5194/acp-17-5623-2017>, 2017.

969 Peng, H., Hu, X., Ai, W., Qiao, J., and Zhao, X.: Effects of fine and coarse aerosols on the summer  
970 precipitation structure and microphysics over the yangtze river delta region, *Atmospheric*  
971 *Research*, 326, 108277, <https://doi.org/10.1016/j.atmosres.2025.108277>, 2025.

972 Pravia-Sarabia, E., Montávez, J. P., Halifa-Marin, A., Jiménez-Guerrero, P., and Gomez-Navarro, J.  
973 J.: The role of aerosol concentration on precipitation in a winter extreme mixed-phase system:  
974 The case of storm filomena, *Remote Sensing*, 15, 1398, <https://doi.org/10.3390/rs15051398>,  
975 2023.

976 Ramanathan, V., Crutzen, P. J., Kiehl, J. T., and Rosenfeld, D.: Aerosols, Climate, and the  
977 Hydrological Cycle, *Science*, 294, 2119–2124, <https://doi.org/10.1126/science.1064034>,  
978 2001.

979 Riemer, M., Montgomery, M. T., and Nicholls, M. E.: A new paradigm for intensity modification  
980 of tropical cyclones: Thermodynamic impact of vertical wind shear on the inflow layer,  
981 *Atmos. Chem. Phys.*, 10, 3163–3188, <https://doi.org/10.5194/acp-10-3163-2010>, 2010.

982 Rosenfeld, D., Lohmann, U., Raga, G. B., O’Dowd, C. D., Kulmala, M., Fuzzi, S., Reissell, A.,  
983 and Andreae, M. O.: Flood or Drought: How Do Aerosols Affect Precipitation?, *Science*, 321,  
984 1309–1313, <https://doi.org/10.1126/science.1160606>, 2008.

985 Shao, H. and Liu, G.: Why is the satellite observed aerosol’s indirect effect so variable?,  
986 *Geophysical Research Letters*, 32, <https://doi.org/10.1029/2005GL023260>, 2005.

987 Snively, D. V. and Gallus, W. A.: Prediction of Convective Morphology in Near-Cloud-Permitting  
988 WRF Model Simulations, *Weather and Forecasting*, 29, 130–149,  
989 <https://doi.org/10.1175/waf-d-13-00047.1>, 2014.

990 Stevens, B. and Feingold, G.: Untangling aerosol effects on clouds and precipitation in a buffered  
991 system, *Nature*, 461, 607–613, <https://doi.org/10.1038/nature08281>, 2009.

992 Stier, P., van den Heever, S. C., Christensen, M. W., Gryspeerdt, E., Dagan, G., Saleeby, S. M.,  
993 Bollasina, M., Donner, L., Emanuel, K., Ekman, A. M. L., Feingold, G., Field, P., Forster, P.,  
994 Haywood, J., Kahn, R., Koren, I., Kummerow, C., L’Ecuyer, T., Lohmann, U., Ming, Y.,  
995 Myhre, G., Quaas, J., Rosenfeld, D., Samset, B., Seifert, A., Stephens, G., and Tao, W.-K.:  
996 Multifaceted aerosol effects on precipitation, *Nat. Geosci.*, 17, 719–732,  
997 <https://doi.org/10.1038/s41561-024-01482-6>, 2024.

998 Storer, R. L., Van Den Heever, S. C., and Stephens, G. L.: Modeling Aerosol Impacts on  
999 Convective Storms in Different Environments, *Journal of the Atmospheric Sciences*, 67,

1000 3904–3915, <https://doi.org/10.1175/2010jas3363.1>, 2010.

1001 Sun, N., Fu, Y., Zhong, L., and Li, R.: Aerosol effects on the vertical structure of precipitation in  
1002 east China, *npj Clim Atmos Sci*, 5, 60, <https://doi.org/10.1038/s41612-022-00284-0>, 2022.

1003 Sun, Y. and Zhao, C.: Distinct impacts on precipitation by aerosol radiative effect over three  
1004 different megacity regions of eastern China, *Atmos. Chem. Phys.*, 21, 16555–16574,  
1005 <https://doi.org/10.5194/acp-21-16555-2021>, 2021.

1006 Sun, Y., Dong, X., Cui, W., Zhou, Z., Fu, Z., Zhou, L., Deng, Y., and Cui, C.: Vertical Structures of  
1007 Typical Meiyu Precipitation Events Retrieved From GPM-DPR, *JGR Atmospheres*, 125,  
1008 <https://doi.org/10.1029/2019jd031466>, 2020.

1009 Sun, Y., Wang, Y., Zhao, C., Zhou, Y., Yang, Y., Yang, X., Fan, H., Zhao, X., and Yang, J.: Vertical  
1010 Dependency of Aerosol Impacts on Local Scale Convective Precipitation, *Geophysical  
1011 Research Letters*, 50, <https://doi.org/10.1029/2022gl102186>, 2023.

1012 Twomey, S.: Pollution and the planetary albedo, *Atmospheric Environment (1967)*, 8, 1251–1256,  
1013 [https://doi.org/10.1016/0004-6981\(74\)90004-3](https://doi.org/10.1016/0004-6981(74)90004-3), 1974.

1014 Wang, Z., Hu, X., Ai, W., Qiao, J., and Zhao, X.: Microphysical characteristics of monsoon  
1015 precipitation over yangtze-and-huai river basin and south China: A comparative study from  
1016 GPM DPR observation, *Remote Sens.*, 16, 3433, <https://doi.org/10.3390/rs16183433>, 2024.

1017 Wen, L., Chen, G., Yang, C., Zhang, H., and Fu, Z.: Seasonal variations in precipitation  
1018 microphysics over East China based on GPM DPR observations, *Atmospheric Research*, 293,  
1019 106933, <https://doi.org/10.1016/j.atmosres.2023.106933>, 2023.

1020 Xi, J., Li, R., Fan, X., and Wang, Y.: Aerosol effects on the three-dimensional structure of  
1021 organized precipitation systems over Beijing-Tianjin-Hebei region in summer, *Atmospheric  
1022 Research*, 298, 107146, <https://doi.org/10.1016/j.atmosres.2023.107146>, 2024.

1023 Xi, J., Wang, Y., Li, R., Wu, B., Fan, X., Ma, X., and Meng, Z.: The impact of Sahara dust aerosols  
1024 on the three-dimensional structure of precipitation systems of different sizes in spring,  
1025 *EGUsphere*, 1–30, <https://doi.org/10.5194/egusphere-2025-2799>, 2025.

1026 Xiao, Y., Zhang, J., Zhu, J., and Dai, Q.: Exploration of aerosol-precipitation relationships under  
1027 different climate regimes in China, *GIScience & Remote Sensing*, 62,  
1028 <https://doi.org/10.1080/15481603.2025.2457992>, 2025.

1029 Xie, X., Liu, X., Peng, Y., Wang, Y., Yue, Z., and Li, X.: Numerical simulation of clouds and  
1030 precipitation depending on different relationships between  
1031 aerosol and cloud droplet spectral dispersion, *Tellus B: Chemical and Physical Meteorology*,  
1032 65, 19054, <https://doi.org/10.3402/tellusb.v65i0.19054>, 2013.

1033 Yu, H.-R., Zhang, Y.-L., Cao, F., Yang, X.-Y., Xie, T., Zhang, Y.-X., and Xue, Y.: Gas-to-particle  
1034 partitioning of atmospheric water-soluble organic aerosols: Indications from high-resolution  
1035 observations of stable carbon isotope, *Atmospheric Environment*, 327, 120494,  
1036 <https://doi.org/10.1016/j.atmosenv.2024.120494>, 2024.

1037 Zhai, H., Yao, J., Wang, G., and Tang, X.: Spatio-Temporal Characteristics and Variation Pattern of  
1038 the Atmospheric Particulate Matter Concentration: A Case Study of the  
1039 Beijing–Tianjin–Hebei Region, China, *Atmosphere*, 13, 120,  
1040 <https://doi.org/10.3390/atmos13010120>, 2022.

1041 Zhang, J., Gao, Z., and Li, Y.: Deep-Learning Correction Methods for Weather Research and  
1042 Forecasting (WRF) Model Precipitation Forecasting: A Case Study over Zhengzhou, China,  
1043 *Atmosphere*, 15, 631, <https://doi.org/10.3390/atmos15060631>, 2024.

1044 Zhao, C., Klein, S. A., Xie, S., Liu, X., Boyle, J. S., and Zhang, Y.: Aerosol first indirect effects on  
1045 non-precipitating low-level liquid cloud properties as simulated by CAM5 at ARM sites,  
1046 Geophysical Research Letters, 39, <https://doi.org/10.1029/2012GL051213>, 2012.

1047 Zhao, C., Lin, Y., Wu, F., Wang, Y., Li, Z., Rosenfeld, D., and Wang, Y.: Enlarging Rainfall Area  
1048 of Tropical Cyclones by Atmospheric Aerosols, Geophysical Research Letters, 45,  
1049 8604–8611, <https://doi.org/10.1029/2018GL079427>, 2018.

1050 Zhao, C., Yang, Y., Fan, H., Huang, J., Fu, Y., Zhang, X., Kang, S., Cong, Z., Letu, H., and  
1051 Menenti, M.: Aerosol characteristics and impacts on weather and climate over the Tibetan  
1052 Plateau, Natl Sci Rev, 7, 492–495, <https://doi.org/10.1093/nsr/nwz184>, 2020.

1053 Zhao, C., Sun, Y., Yang, J., Li, J., Zhou, Y., Yang, Y., Fan, H., and Zhao, X.: Observational  
1054 evidence and mechanisms of aerosol effects on precipitation, Science Bulletin, 69,  
1055 1569–1580, <https://doi.org/10.1016/j.scib.2024.03.014>, 2024.

1056 Zhao, J., Li, T., Shi, K., Qiao, Z., and Xia, Z.: Evaluation of ERA-5 precipitable water vapor data  
1057 in plateau areas: A case study of the northern qinghai-tibet plateau, Atmosphere, 12, 1367,  
1058 <https://doi.org/10.3390/atmos12101367>, 2021.

1059 Zhao, X., Zhao, C., Chi, Y., Yang, J., Sun, Y., Yang, Y., and Fan, H.: Different Impacts of Aerosols  
1060 on Cloud Development over Land and Ocean Regions in East China, Adv. Atmos. Sci., 42,  
1061 731–743, <https://doi.org/10.1007/s00376-024-4165-z>, 2025.

1062 Zhou, J., Zhao, W., Fang, B., Xu, X., Wang, S., Liu, Q., Zhang, W., and Chen, W.:  
1063 Unmanned-aerial-vehicle-borne cavity enhanced albedometer: A powerful tool for  
1064 simultaneous in-situ measurement of aerosol light scattering and absorption vertical profiles,  
1065 Opt. Express, 31, 20518, <https://doi.org/10.1364/oe.493696>, 2023.

1066 Zhou, L., Xu, G., Xiao, Y., Wan, R., Wang, J., and Leng, L.: Vertical structures of abrupt heavy  
1067 rainfall events over southwest China with complex topography detected by dual-frequency  
1068 precipitation radar of global precipitation measurement satellite, Intl Journal of Climatology,  
1069 42, 7628–7647, <https://doi.org/10.1002/joc.7669>, 2022.

1070 Zhu, H., Zhao, H., Yang, S., Zhou, R., Wang, Y., Zou, Y., Zhao, C., and Li, R.: Smoke aerosols  
1071 elevate precipitation top and latent heat to the upper atmosphere globally, npj Clim Atmos Sci,  
1072 8, <https://doi.org/10.1038/s41612-025-01047-3>, 2025.

1073 Zhuang, Y., Lin, T., Zhou, W., Guo, Z., and Wang, F.: Characteristics of temporal variations in  
1074 organic and elemental carbon aerosols from Eastern China in 2011–2020, Journal of  
1075 Environmental Sciences, 155, 583–596, <https://doi.org/10.1016/j.jes.2024.05.037>, 2025.

1076